Modeling the Anchoring and Performance of Downhole Equipment Using an Extended Gurson Model

Mostafa E. Mobasher[1*, †], Peter Taylor[1], Pawel B. Woelke[1], Norman A. Fleck[2], John W. Hutchinson[3], Allan Zhong[4]

[1] Thornton Tomasetti, Applied Science, New York, NY, 10005, USA

[2] Department of Engineering, University of Cambridge, Cambridge CB2 1PZ, UK

[3] School of Engineering and Applied Sciences, Harvard University, USA

[4] Halliburton, 2610 E Beltline Road, Carrollton, TX, 75005, USA

Key words: downhole equipment, ductile failure, Gurson model, indentation, shear loading

Abstract

In oil and gas (O&G) exploration the well casing, in the form of a long steel tube, maintains the opening of the drilled well hole. Mechanical equipment is often inserted into the well for the purpose of well monitoring, pressure control and various operations. This downhole equipment may be mechanically connected to the pipe casing by the outward radial motion of anchoring teeth such that the inner wall casing is indented. The connection between the tool and the casing must support significant mechanical loads in the longitudinal (axial) direction of the casing, i.e. transverse to the direction of indentation, while minimizing the indentation depth in order to preserve the stiffness and strength of the casing. Consequently, a determination of the ultimate strength of the connection is of critical importance. Failure of this connection involves intense shear of the inner wall of the casing, akin to a machining operation. The critical load for axial slip can be determined experimentally or numerically (or by combination of both). In this study, detailed simulations are performed using the shear-extended GTN (Gurson-Tvergaard-Needleman) model. The choice of model is motivated by the need to accurately the extensive plastic deformation associated with indentation as well as shear-dominated ductile failure on a sub-millimeter scale.

The shear-extended GTN model requires a careful calibration of the model parameters by an accurate measurement of the material response. Accordingly, the casing steel was characterized by appropriate measurements under a range of stress states. The calibrated model was used to

*: *Corresponding Author*

†: *Currently at Civil and Urban Engineering Department, New York University Abu Dhabi, Abu Dhabi P.O. Box 129188, United Arab Emirates*

investigate an idealized two-dimensional representation of the anchoring problem, with a focus on the effect of indentation depth upon connection strength. Both the indentation of the casing inner wall by the anchoring teeth and the subsequent shear of the casing wall were simulated in detail to determine the load required to initiate and progress slip of the anchoring teeth. The results of these analyses show that the connection strength increases linearly with increasing indentation depth.

1. Introduction

In the oil and gas (O&G) industry it is often necessary to install equipment inside the well bore, or 'downhole', after the well has been drilled and lined with a steel casing. There is a wide range of uses of downhole tools inside the casing, which include the monitoring of casing motion and deformation, fluid pressure monitoring and fluid control [1]. Downhole tools are fixed in position by direct anchoring into the inner wall of the casing. This process (often referred to as setting, see Fig. 1 [2] & [3]) involves the radial expansion of connecting elements of the tool called slips. These slips feature externally protruding teeth that are forced into the inner wall of the downhole casing; the casing also expands radially. Indentation by the tool's teeth into the inner wall of the casing provides an effective shear connection, such that the weight of the tool and ancillary equipment are supported. Typically, the teeth are designed to act as rigid indenters into the steel casing with different materials used to achieve this goal [2] & [3]. The integrity of the tool-casing connection is critical to the ability to perform various downhole operations and the design of these operations requires a knowledge of the ultimate strength of this connection. Additional background information on the downhole equipment and the anchoring process can be found in [2] & [3].

The general principle of the anchoring process as discussed above is used in multiple industries. However, the details of the tool are usually customized to support specialist operations. Multiple manufacturers offer unique designs that are often based on proprietary solutions. Consequently, standardization is difficult and a determination of the connection strength requires controlled experimental testing, possibly of the entire assembly (i.e. casing and the tool) supported by detailed simulations. In this paper, we focus on detailed simulation of the indentation and shear by the teeth into the casing to determine the connection strength as a function of indentation depth.

An accurate determination of the ultimate strength of the connection by simulation requires a detailed knowledge of material failure. Extensive plastic deformation of the casing material during indentation must also be well represented. The casing material is subjected to a complex and non-

proportional loading that involves extensive compression during indentation, followed by intense machining . Previous studies attempted to model the setting process and predict the connection strength using detailed FEM models. However, the ductile failure representations were limited to von Mises plasticity ([4], [3]). Zhong et al [5] highlighted the need to address shear failure to achieve good agreement with experimentally observed behavior. Additionally, since the teeth are relatively small (~1mm) compared to the casing thickness, the relevant processes occur on the sub-millimeter scale. Thus, an advanced micromechanics-based constitutive model is best suited to resolve material behavior.

The micromechanics-based Gurson-Tvergaard-Needleman (GTN) ([6], [7], [8, 9]) model is an ideal tool for the simulation of the anchoring (teeth indentation) and shearing processes. The GTN model has been formulated to describe ductile fracture under axisymmetric stress states, thereby accounting for the effect of stress triaxiality, as defined by the ratio of mean and effective stress. More recently, detailed experimental studies of ductile fracture by Bao and Wierzbicki [10] and by Barsoum and Faleskog [11] reveal that, in addition to the first two stress invariants (mean and effective stress), the third invariant of deviatoric stress is also important, especially under shear-dominated stress states. This third stress invariant is commonly parameterized by the so-called Lode angle. Based on the experiments of [10,11], as well as upon fundamental investigations of void growth mechanics (Needleman et al. [12]; Fritzen et al. [13]; Nielsen and Tvergaard [14]; Tvergaard [15], [16]), Nahshon and Hutchinson [17] proposed an extension of the micromechanical GTN model to account for shear fracture. Their shear-extended model features a phenomenological shear damage function dependent on the omega parameter, which can be regarded as a normalization of the Lode angle.

An identification of the parameters for the GTN model presents a challenge, as discussed extensively by Hojo and Watanabe [18]. While unit cell simulations can be used to calculate the appropriate values for some of the parameters as well as relationships between them, a complete calibration of the model requires extensive experimental testing as shown by Faleskog et al. [19] and Kim et al [20]. A combination of tensile and shear tests is necessary, with the test specimens and loading carefully designed to promote failure under specific stress states (e.g. Faleskog and Barsoum [21], Xue et al [22], and Scales et al. [23]).

In the present study, a shear-extended GTN model is used to investigate the performance of the downhole anchored connection. Multiple tensile and torsional specimens were used to characterize

the casing material and to calibrate the model parameters. After suitable calibration, the model was used to investigate the strength of the tool-casing connection in two steps. Indentation of the tool's teeth into the inner wall of the casing was first simulated, followed by the application of a monotonically increasing displacement of the tool in the axial direction of the casing (transverse to the indentation direction). The force required to initiate and progress the tool's slippage along the casing was then calculated. While this approach was developed specifically to address the problem described above, it can also be used to model other applications such as intense wear and/or machining processes.

The paper is organized in six sections. Following the introduction, a brief overview of the shear extended GTN model formulation is given in Section 2. Sections 3 and 4 describe the experimental testing procedures and calibration of the model parameters, respectively. Section 5 presents the details of the investigation of the downhole tool-casing connection strength through combined simulation of the indentation process followed by shear. Conclusions are given in Section 6.

2. The shear-extended GTN model

The shear-extended GTN model [17] is now summarized. To begin, the original GTN model ([6], [7], [8], [9]) is given by:

$$F(\sigma_e, \sigma_m) = \left(\frac{\sigma_e}{\sigma_M}\right)^2 + 2q_1 f^* \cosh\left(\frac{3q_2}{2}\frac{\sigma_m}{\sigma_M}\right) - \left(1 + q_3 f^{*2}\right) \tag{1}$$

where, $\sigma_m = \sigma_{kk}/3$ is the mean stress and $\sigma_e = \sqrt{3 s_{ij} s_{ij}/2}$ is the von Mises effective stress; the stress deviator reads $s_{ij} = \sigma_{ij} - (1/3)\sigma_{kk}\delta_{ij}$ in terms of the Cauchy stress σ_{ij}. The equivalent strength of the undamaged matrix is denoted by σ_M, f^* is closely related to the void volume fraction f (as explained below with reference to Equation 4) and the parameters q_1, q_2 and q_3 are model-fitting parameters as proposed by Tvergaard [6]. It is useful to note that the yield surface as described in Equation (1) reduces to the von Mises yield surface when $f^* = 0$, or $q_1 = q_2 = q_3 = 0$. Upon ignoring void nucleation, the evolution of the void volume fraction is ([17], [24]):

$$\dot{f} = (1 - f)\dot{\varepsilon}^P_{kk} + k_\omega f \omega(\sigma_{ij}) \frac{s_{ij}}{\sigma_e} \dot{\varepsilon}^p_{ij} \tag{2}$$

where the plastic strain tensor is ε^p_{ij}, the volumetric plastic strain is ε^p_{kk}, the over-dot denotes the first derivative in time, and the material parameter k_ω defines the damage growth rate in pure shear. For the problem of the present study, void growth is the dominant mechanism and void

nucleation is neglected (but with the assumption of a finite initial void volume fraction). This assumption allows a reduction in the number of experiments for a full calibration of the model, including the nucleation term [25]. The first term on the right-hand side of Equation (2) accounts for void growth rate associated with volumetric straining. The second term accounts for the effect of shear deformation, including void rotation, lengthening and subsequent softening, on the evolution of damage. We note that the shear extension is phenomenological and leads to the loss of physical interpretation of f as the void volume fraction. The stress invariant $\omega(\sigma_{ij})$ is defined by:

$$\omega(\sigma) = 1 - \left(\frac{27J_3}{2\sigma_e^3}\right)^2 \tag{3}$$

where J_3 is the 3rd deviatoric stress invariant, such that $3J_3 = s_{ij}s_{ik}s_{jk}$. The value of ω lies in the range $0 \leq \omega \leq 1$ such that ω=0 for an axisymmetric stress state and ω=1 for a shear stress and superposed hydrostatic stress [17]. The invariant ω is related to the Lode angle (L) by

$$\omega = \frac{27(L^2-1)^2}{(3+L^2)^3} \tag{4}$$

where L is given by

$$L = \frac{2\sigma_{II} - \sigma_I - \sigma_{III}}{\sigma_I - \sigma_{III}} \tag{5}$$

and lies in the range $-1 \leq L \leq 1$ [22]. A widely used approach to account for the onset of void coalescence is included [24]:

$$f^* = \begin{cases} f & f \leq f_c \\ f_c + \dfrac{\bar{f}_f - f_c}{f_f - f_c}(f - f_c) & f_c < f < f_f, \quad \bar{f}_f = \dfrac{q_1 + \sqrt{q_1^2 + q_3}}{q_3} \\ \bar{f}_f & f \geq f_f \end{cases} \tag{6}$$

where f_c is the critical void ratio at which void coalescence begins, and f_f is the final void ratio at which the material element has zero strength.

The flow rule and hardening behavior adopted in this paper follows the original GTN model. The plastic strain rate $\dot{\varepsilon}_{ij}^p$ is given by the normality relation:

(7)

$$\dot{\varepsilon}_{ij}^{p} = \dot{\lambda}\frac{\partial F}{\partial \sigma_{ij}} = \dot{\lambda}\alpha_{ij}$$

where $\dot{\lambda}$ is the plastic strain-rate multiplier and the normal to the yield surface α_{ij} is defined by:

$$\alpha_{ij} = \frac{3s_{ij}}{\sigma_M^2} + \frac{f^* q_1 q_2}{\sigma_M}\sinh\left(\frac{3q_2\sigma_m}{2\sigma_M}\right)\delta_{ij} \tag{8}$$

The plastic work increment in the matrix material is related to the macroscopic plastic work increment via:

$$(1-f^*)\sigma_M \dot{\varepsilon}_M^p = \sigma_{ij}\dot{\varepsilon}_{ij}^p \tag{9}$$

Consequently, the matrix stain hardens at a rate $\dot{\sigma}_M$ such that:

$$\dot{\sigma}_M = \frac{h_M \sigma_{ij}\,\dot{\varepsilon}_{ij}^p}{(1-f^*)\sigma_M} \tag{10}$$

where h_M is the plastic modulus of the matrix material in uniaxial tension, and is stated in terms of the true stress in uniaxial tension and the resulting logarithmic plastic strain:

$$h_M = \frac{d\sigma_M}{d\varepsilon_M^p} \tag{11}$$

The above equations, which describe the hardening behavior, are identical to those of the original GTN model with the exception of an additional term for shear damage in Equation (2).Additional definitions required to compliment the definition of the model are detailed in [26].

3. Experimental Protocol

Detailed tests are required to characterize the material and calibrate model parameters. In this study, we follow the approach of [26] and [22]. The following experiments were performed:

A. Tensile tests on round dogbone (RDB) specimens at several strain rates.

B. Tensile and torsion tests on round notch bar (RNB) specimens of selected notch radius.

The test specimens were machined from an AISI 4140 steel casing (of outer diameter 175 mm, and wall thickness 15.9 mm). The deformation within the gauge length was observed by a combination of clip gauge, laser gauge and a 3D Digital Image Correlation (DIC) system. Additional information on specimen manufacture and the instrumentation employed is given in supplemental material.

3.1. Round dogbone (RDB) specimen

An RDB specimen was machined, following ASTM A370 [27], to a length of 150 mm, a gauge diameter of 6 mm and a gauge section length of 30 mm. The tensile test was performed at 3 strain rates: 10^{-5} s^{-1}, 10^{-4} s^{-1} and 10^{-3} s^{-1}. A laser gauge and a clip gauge were used to measure axial strain in the gauge section. The engineering strain up to about 1% was measured by a clip gauge (of gauge length 12.5mm), whereas engineering strain at larger values (up to 10%) were measured using a laser gauge (of gauge length 23mm). The clip gauge is vulnerable to overload when the specimen undergoes a tensile dynamic instability at the end of the test, and so it was necessary to remove the clip gauge from the specimen prior to fracture.

The engineering stress versus engineering strain curve is plotted in Fig. 2 for the 3 different strain rates. As shown in Fig. 2, the steel displayed minimal rate sensitivity over the given range. A 'cup and cone' type of ductile failure occurred within the neck as shown on the macro fracture surface in Fig. 3. The failure mechanism was microvoid coalescence.

3.2. Round Notch Bar (RNB) – Tension

RNB specimens with a range of notch sizes were tested, see Fig. 4; the aim was to create a range of triaxiality of stress-state in the failure zone as discussed in [21] and [22]. Each specimen was instrumented with a clip gauge and a laser gauge straddling the notch in order to measure the opening of the notch. In addition, a virtual extensometer was used to monitor the evolution of strain within the notch from the DIC measurements. The gauge length of the virtual extensometer is listed in Table 1 for different notch sizes. In each test, the load was first applied up to a value close to the expected maximum load, or until the paint speckle cracks. The specimen was then unloaded, repainted, and loaded until failure. This procedure was followed to protect the clip gauge from the possibility of over-extension and to ensure that the DIC measurements were not affected by paint cracking. Following removal of the clip gauge, the notch opening during the reload tests was measured by the laser gauge.

Snapshots from DIC imaging at localization and failure for the 1mm notch test are shown in Figs. 5a and 5b, respectively. Figure 6 shows the load versus extension response of the notched bars (3mm and 9mm radius) in tension. The engineering strain at localization is listed in Table 1 for the different specimen sizes. The onset of localization is defined as the instant at which large local strains begin to develop in the middle of the notch, and softening ensues shortly thereafter. The onset of localization is marked on Figs. 6 and 7. As expected, and observed in previous studies,

the failure strain is higher for the blunter notches (larger root radius); this is attributed to delayed localization of the root section.

3.3. Round notch bar (RNB) – Torsion

A similar set of RNB specimens was tested in torsion. The specimen geometries in Fig. 4 were modified to have 12mm x 12mm square ends for grippage. The torque versus end-rotation response for the 3 notch sizes is shown in Fig. 7. The shear strain at peak torque is almost independent of notch root radius, as summarized in Table 1. The shear strain is defined as

$$\gamma = \frac{\partial v}{\partial x} \tag{12}$$

where x is the axial direction of the specimen and ν is the displacement in the circumferential direction. Note that the 1mm notch test used a virtual extensometer of gauge length 0.5 mm while the 3 mm and 9 mm notch tests used virtual extensometers of gauge length 1 mm. Snapshots of the DIC imaging at localization and failure for the 9 mm notch test are shown in Figs. 8a and 8b, respectively. The above results point to the fundamental differences between failure in tension and in shear. The localization strain in tension is much more sensitive to notch size than in torsion. Failure in tension leads to the cup and cone typical ductile fracture, while the shear-torsion failure leads to a planar shear fracture. The variation of the notch size in tension has direct influence on the stress-state inside the notch, and consequently upon the failure profile and fracture strain. This observation is supported by simulations as reported below.

4. Model Calibration

The shear extended GTN model contains several parameters that define the ductile fracture response; this allows the model to be used to analyze a wide range of loading regimes [17]. Once the model parameters have been calibrated by appropriate experiments, the model can be used to represent the initiation and propagation ductile fracture under multi-axial loading. In this section, the process of calibrating the model parameters from the experimental results of Section 3 is discussed. Based on the lessons learned from previous studies ([26], [21], [22]) the calibration process was carried out in the following order:

1. Calibration of the hardening curve, hardening parameters (q_1 , q_2, and q_3) and initial void ratio based on RDB tension response.

2. Calibration of the failure parameters: critical and final void ratio (f_c and f_f) and shear factor k_ω based on RNB tension and torsion data.

Given the complexity of the model, the relatively large number of parameters and experimental data points, it is expected that the calibrated parameter set is non-unique. The issue of non-uniqueness of GTN parameter sets has been documented elsewhere [28]. Here, the performance of calibrated parameter sets was evaluated through four evaluation criteria:

- Yield force (in tension) or torque (in torsion)
- Maximum force (in tension) or torque (in torsion)
- Maximum displacement (in tension) or rotation (in torsion)
- Mechanical energy dissipated

The initial values of the model parameters were selected based on published guidelines [21, 26, 22]. The optimization operation was performed by minimizing the error between the measured and calculated responses across all types of specimens used on the experimental study. The error was defined as a linear combination of the four evaluation criteria defined above. In addition, the parameters were optimized to represent specific aspects of the measured response such as necking and localization prior to crack initiation and propagation.

The model was implemented as an explicit user material (VUMAT) [29] within the commercial finite element code Abaqus Explicit. Element deletion was employed, with the deletion criterion based on the final value of the void ratio f_f as defined in Equation (6). Mass scaling was used via an artificially higher material density in order to increase the value of stable time-step in the explicit calculations [29], [30]. In each simulation, several initial trials were performed to ensure that the mass scaling does not significantly degrade the accuracy of the simulation results. It is recognized that mesh-dependence has been observed in the softening regime of GTN models following void coalescence, leading to fracture propagation; in the absence of an explicit material length scale, it is necessary to keep the element size to be of the same order of magnitude as the size of the pre-existing voids [26]. The element size in the following simulations was kept in the range of 40 to 150 μm, as suggested in previous studies ([31], [32], [26], [33]). Details of finite element model used to represent each specimen are given in supplemental material.

4.1. Hardening Curve and Parameters

The plastic response in the shear modified GTN model is dictated by the model parameters: the initial void ratio f_0 and the q parameters. Note that, in the absence of voids ($f_0 = 0, f = 0$), the GTN model reduces to von Mises plasticity. Accordingly, in order to isolate the effect of the hardening curve on the plastic response, the initial calibration of the hardening curve was performed assuming that voids are absent, i.e. $f_0 = 0, f = 0$. This allows calibration of the yield surface of the undamaged matrix material [24, 26]. The data retrieved from the RDB tensile test was used to calibrate the hardening curve. The primary reason is that the RDB specimen does not contain notches and provides an average representative undamaged stress-strain behavior up to the onset of localization. The hardening curve is obtained by suitable extrapolation of the true stress versus true (logarithmic) strain response in uniaxial tension between yield and maximum loads. Two possible options of extrapolated hardening curves were investigated: (i) extrapolation along the final slope of the curve at the peak load or (ii) an extension of the curve with a slope that is half that of (i). The two options are plotted in Fig. 9. In the following discussions, these options will be denoted as (i) "High HC" and (ii) "Low HC".

The plots in Fig. 10 show that the force versus displacement prediction using the High HC aligns with that of the experimental curve. We emphasize that this prediction assumes that voids are absent, thus it is expected that the simulated response will demonstrate lower resistance (force) after voids have been introduced in the GTN model. In Fig. 10, the Low HC curve undershoots the response in the experimental curve. Despite the conclusion that the High HC plot leads to a better match in the RDB simulations, we will show below in section 4.2 that the Low HC gives a more accurate match to experimental data in shear loading cases.

The set of values of the q parameters ($q_1 = 1.5,\ q_2 = 1.0$ and $q_3 = 2.25$) was taken from previous studies [6], [7]. Fig. 11 shows the effect of increasing f_0 from 0.1% to 0.9% upon the High HC and Low HC responses. A combination of Low HC and f_0 = 0.9% leads to considerable undershoot of the force-displacement response.

4.2. Failure parameters

A calibration of the void ratios (f_c and f_f) and the shear damage factor k_ω is central to the description of the multiaxial loading response of the model. Following an initial parameter sensitivity study, it was concluded that four sets of values provide the best match between experimental and simulated responses, see Table 2. Detailed force versus displacement and torque

versus end rotation plots, showing the sensitivity to the choice of parameters, are provided in supplemental material.

4.3. Performance evaluation

The performance of the four parameter sets is evaluated using the above-mentioned criteria. A graphical representation of the evaluation is shown in Fig. 12. The numerical comparison indicates that Set 4 exhibits the smallest combination of errors. Although Set 4 provides the best overall fit, other Sets may provide better representation in specific cases. For example, Set 3 is a viable alternative for the modeling of the torsional responses.

5. Assessment of anchored connection strength

5.1. The Finite Element Model

As previously discussed the downhole equipment anchoring process involves the radial movement of protruding teeth of the slips into the inner wall of the downhole casing. During this indentation event the casing expands radially but the loading is not truly axisymmetric, since the teeth are not continuous around the circumference (see Fig .1). Additionally, casing expansion is an important element of the process and the complete evaluation of the connection strength would require an accurate representation of this expansion. However, a detailed assessment only makes sense for a specific scenario since the casing expansion is dependent upon the casing material and geometry in addition to the properties of the well, which acts as an elastic foundation for the casing. This is not the objective of this work. Rather, we aim to investigate the fundamental dependence of connection strength upon indentation depth, and this can be achieved by assuming plane strain conditions and no expansion of the casing . An extension of this work to include the full 3D representation with the radial expansion is future work, beyond the scope of the present study.

The 2D plane strain finite element model used to assess the tool-casing connection strength as a function of indentation depth is shown in Fig. 13. The average element size in the refined portion of the model, i.e. in the region of indentation, is 75μm. Reduced integration 8-node continuum elements (ABAQUS C3D8R elements) were used throughout the finite element model. The model is one element deep in the out-of-plane-direction, with symmetry boundary conditions applied to the planar faces (near and far sides) to enforce plane strain. The bottom, right and left boundaries were supported by rollers. The overall extent of the model was sufficient to ensure that boundary

effects did not influence the local response around the teeth, and did not affect the overall force versus displacement response.

The tool is treated as rigid and the contact condition includes a nominal steel-on-steel Coulomb friction coefficient of 0.6 (a sensitivity study showed that the response is not highly sensitive to the choice of coefficient of friction). The tooth internal angle is 54°; this choice is commonly used in practice. The model can be modified to represent other angles in a straightforward fashion; however, this parametric study is beyond the scope of this paper.

The loading was applied in two-steps:

1) the indenter (rigid tool) was pushed into the casing material along the y-direction (see Fig. 13);

2) the slips with the indenters (teeth) were translated in the x-direction (transverse to the indentation direction) to represent the loading on the anchored connection.

Displacement controlled loading was used with a monotonic increase and the number of the load steps automatically controlled by the stable time step. Large deformation elements were used to account for the expected geometric non-linearity. Two material models were considered for the steel specimen:

1. the shear-extended GTN model with calibrated parameters as defined in Section 4. Element deletion is set to occur when the void ratio reaches the final void ratio f_f defined in Equation (6);

2. the von Mises plasticity model (that is, J2 flow theory) with Low HC and element deletion criterion based on the critical level of the equivalent plastic strain (i.e. 200%). The value of 200% was chosen to resemble the equivalent plastic strain in most severely strained elements in Set 4 RNB-Torsion simulations at failure.

A comparison between the shear-extended GTN and von Mises models is discussed in Section 5.2. The sensitivity of indentation force and connection strength to the number of indenting teeth is explored in Section 5.3. We note that the maximum indentation depth in Sections 5.2 and 5.3 exceeds the typical depth applied in reality; this is done so to reveal the stress-state around the teeth in detail. In practice, a large indentation depth may lead to degradation of casing integrity. The effect of indentation depth on the shear resistance of the connection is investigated in Section 5.4.

5.2. Predictions by the shear-extended GTN and von Mises material descriptions

The equivalent plastic strain after indentation and slippage, as calculated using the extended GTN model and the von Mises model are plotted in Fig. 14a-b and 14 c-d respectively. The shear force versus tool horizontal displacement is reported in Fig. 15 for both models. Quantitative differences are expected in the overall force-displacement due to the overall changes in the geometric design. However, variations in the design of the anchoring tool are expected to yield qualitatively similar results, and in the width of the shear planes in Fig. 14 will remain representative because this is primarily controlled by material behavior.

The response calculated using the shear-extended GTN model exhibits significantly more hardening than the corresponding solution obtained using the von Mises model. Since failure in the von Mises model is approximated simply by the removal of an element once its equivalent plastic strain has reached a critical level of 200%, progressive failure occurs along the shearing line (i.e. unzipping) as observed in other studies ([2], [4] and [3]). But this mechanism neither matches other observations ([5], [34]) nor field observations, and this motivates a more detailed investigation using the extended GTN model, given its ability to account for the triaxial stress state on ductile failure.

Initial simulations using the calibrated extended GTN model experienced computational challenges. As shown in Fig. 14b and 16b, elements in contact with the tool experienced extreme deformation, which led to increased run time and convergence issues. Compression of these elements during indentation led to a reduction in void ratio f (Eq. 3), which corresponds to a gradual reduction in void size until the voids vanish (Fig. 16a and 16b). This behavior is unphysical since, in reality, voids flatten into crack-like features under hydrostatic compression rather than shrink uniformly ([35], [36]). In order to address this challenge, an additional condition was introduced: $\dot{f} \geq 0$, which prevents the void ratio from dropping below the current value throughout the simulation. The simulations performed using the 'no-void-closure' condition led to improved computational performance with no severe unphysical distortions of the elements. Additionally, the indentation loads and subsequent shear forces were less than those obtained for void shrinkage (Figs. 17 and 18). This response is consistent with the fact that void shrinkage leads to a stiffening response. In the presence of other combinations of volumetric and shear stress states, the introduction of the no void shrinkage condition could alter the void evolution, which was not observed here.

Note too that the Mises model successfully captures the overall force-displacement behavior. For practical applications, a well-calibrated Mises model may require a lower computational cost than the shear-extended GTN model, but full confirmation of this conclusion would require additional investigation.

5.3. Sensitivity of indentation and subsequent shear response to number of teeth

The main objective of the present study is to assess a dependence of the tool-casing connection strength as a function of the indentation depth. It is also of practical importance to determine the shear force per tooth as a function of the number of teeth, with the expectation that it would asymptotically approach a constant value with increasing number of equally spaced teeth. A parametric study was performed to determine the minimum (threshold) number of teeth required in order to attain a constant shear force per tooth of the connection. The parametric study includes 1, 2 and 3 teeth on the side of the tool. As an additional note, it is worth adding that a single tooth with a periodic boundary condition could be analyzed in lieu of analyzing multiple configurations. However, the extent of the movement of each tooth exceeds the spacing between the teeth and therefore the boundary line, which presents significant computation challenges.

Plots of the equivalent plastic strain from the three cases are shown in Fig. 19. The indentation and shear force per tooth are plotted in Fig. 20. Several observations can be made from these figures. First, the most intense local loading occurs near the trailing, leftmost tooth along the shear plane between teeth. The material between the subsequent teeth slides along a shear plane, but localization and fracture occur adjacent to the trailing tooth. It is also noted that the difference between the two teeth and the three teeth is minimal in Fig. 20, which indicates that the use of three teeth is sufficient for the calculation of the indentation and shear force per tooth.

5.4. Relation between shear strength and indentation depth

It is generally recognized that, as the indentation depth increases, the strength of the anchored connection increases but the integrity of the casing decreases. A quantification of the relation between the connection strength and indentation force (applied to set the tool) is an important factor in the design of the connection and casing. The indentation depth was varied by increments of 20% of total tooth depth {that is, 20%, 40%, 60%, 80%, 100%}. Both the shear-extended GTN model and the von Mises model were considered and the shear strength of the connection was

plotted as a function of average indentation force per tooth in each simulation, see Fig. 21. Two values of strength are reported in Fig. 21: the "yield" strength, which is simply the strength recorded at the point in which the shear force displacement response becomes non-linear, and the second is the "maximum strength" which is the force recorded at a shear displacement of 2 mm, as shown in Fig. 18. The plot shows that the relationship between shear strength and indentation force is linear for this 2D plane strain idealization. The shear-extended GTN and von Mises models give similar predictions for the yield load in shear, and this may be adequate for design purposes. Note that the yield and maximum values of shear force almost coincide for the von Mises model, but diverge for the shear-extended GTN model. In broad terms, the shear-extended GTN model suggests that a greater safety margin exists than does the von Mises criterion. We emphasize that these conclusions may be sensitive to the modeling assumptions made here, e.g. the plane strain idealization.

6. Summary and Conclusions

This study introduces a novel approach for the calculation of the strength of downhole tool-casing connection used in the oil and gas industry. The connection was formed by indentation of small-sized (~1mm) teeth into the inner wall of the downhole casing. Given the scale of the teeth as well as the indentation and shearing phenomenon, a high-fidelity micro-scale analysis is required to calculate the connection strength. The calculations presented here were obtained using both the shear-extended GTN material model and the von Mises plasticity model to predict the deformation and failure of the casing material. The study is underpinned by a detailed experimental testing campaign aimed at characterization of the casing material and calibration of the model parameters. The calibrated material model was used to calculate the connection strength in a two-stage simulation: 1) indentation, and 2) slippage of the teeth against the casing (in the longitudinal casing direction) leading to shear failure on the surface of the casing. The simulations were performed using idealized two-dimensional plane strain conditions.

The current study highlights the fact that void growth in an elasto-plastic matrix is irreversible: plastic straining with a high compressive component does not shrink voids but converts them into crack-like features that continue to soften the solid. A straightforward, pragmatic approach to satisfy this requirement, is to enforce that the void volume fraction can never decrease in magnitude, regardless of the loading path, as done herein.

The finite element model developed in this study has been used to perform several parametric studies. First, the number of teeth was varied to investigate the minimum number of teeth required to represent a given connection. The results suggest that two teeth are sufficient to calculate the connection shear strength per tooth. The second parametric study investigated the effect of teeth indentation depth upon anchorage shear strength. We find that the shear strength scales linearly with indentation force. We stress that these findings are for 2D plane strain simulations and more general conclusions require further work.

References

[1] C. H. Gao, R. T. Rajeswaran and E. Y. Nakagawa, "A Literature Review on Smart Well Technology," *Production and Operation Symposium,* March 2007.

[2] Z. Liu, L. Zhang, F. Wang, S. Li, P. Wang, M. Cai, L. Hang, Y. Ma, Z. Ma and B. Yan, "Study on optimization design of permanent packer slip," *Journal of Failure Analysis and Prevention,* vol. 21, pp. 50-60, 2021.

[3] B. Liu, M. Cai, J. Li, Z. Yang and S. Lu, "Application and Analysis of Fracture Simulation of the Slip of the Permanent Packer," *International Conference on Modeling, Simulation, Optimization and Numerical Techniques (SMONT 2019),* pp. 270-274, April 2019.

[4] X. Sun, Y. Dou, H. Song, X. Wang and Y. Cao, "Analysis of the Interaction between Casing and Completion Packer Slip in HPHT Wells," in *2nd International Conference on Machinery, Materials Engineering, Chemical Engineering and Biotechnology,* 2015.

[5] A. Zhong, J. Clemens and M. Mlcak, "Application of Fracture Mechanics for Evaluation and Improvement of Downhole Perforating Tools," in *Simulia Community Conference,* 2014.

[6] V. Tvergaard, "Influence of voids on shear band instabilities under plane strain conditions," *International Journal of Fracture,* vol. 17, no. 4, pp. 389-407, 1981.

[7] V. Tvergaard, "On Localization in ductile materials containing spherical voids," *International Journal of Fracture,* vol. 18, no. 4, pp. 237-252, 1982.

[8] A. Needleman and V. Tvergaard, "An analysis of ductile rupture in notched bars," *Journal of the Mechanics and Physics of Solids,* vol. 32, no. 6, pp. 461-490, 1984.

[9] A. L. Gurson, "Continuum theory of ductile rupture by void nucleation and growth - Part I. Yield criteria and flow rules for porous ductile media," *Journal of Engineering Materials and Technology,* vol. 99, no. 1, pp. 2-15, 1977.

[10] Y. Bao and T. Wierzbicki, "On the cut-off value of negative triaxiality for fracture," *Engineering Fracture Mechanics,* vol. 72, no. 7, pp. 1049-1069, 2005.

[11] I. Barsoum and J. Faleskog, "Rupture mechanisms in combined tension and shear," *International journal of solids and structures,* vol. 44, no. 6, pp. 1768-1786, 2007.

[12] A. Needleman, V. Tvergaard and J. W. Hutchinson, "Void growth in plastic solids," in *Argon A.S. (eds) Topics in Fracture and Fatigue,* New York, Springer, 1992, pp. 145-178.

[13] F. Fritzen, S. Forest, T. Bohlke, D. Kondo and T. Kanit, "Computational homogenization of elasto-plastic porous metals," *International Journal of Plasticity,* vol. 29, pp. 102-119, 2012.

[14] K. L. Nielson and V. Tvergaard, "Failure by void coalescence in metallic materials containing primary and secondary voids subject to intense shearing," *International Journal of Solids and Structures,* vol. 48, no. 9, pp. 1255-1267, 2011.

[15] V. Tvergaard, "Shear deformation of voids with contact modelled by internal pressure," *International Journal of Mechanical Sciences,* vol. 50, no. 10-11, pp. 1459-1465, 2008.

[16] V. Tvergaard, "Behaviour of voids in a shear field," *International Journal of Fracture,* vol. 158, pp. 41-49, 2009.

[17] K. Nahshon and J. W. Hutchinson, "Modification of the Gurson Model for shear failure," *European Journal of Mechanics A/Solids,* vol. 27, pp. 1-17, 2008.

[18] K. Hojo and D. Watanabe, "Application of Gurson Model to Ni-based alloy weld joint pipe with an axial or a circumferential surface flaw: Phase II," in *Proceedings of the ASME 2013 Pressure Vessels and Piping Conference. Volume 3: Design and Analysis*, Paris, 2014.

[19] J. Faleskog, X. Gao and F. Shih, "Cell model for nonlinear fracture analysis – I. Michromechanics calibration," *International Journal of Fracture,* vol. 89, pp. 355-373, 1998.

[20] J. Kim, X. Gao and T. S. Srivatsan, "Modeling of void growth in ductile solids: effects of stress triaxiality and initial porosity," *Engineering Fracture Mechanics,* vol. 71, no. 3, pp. 379-400, 2004.

[21] J. Faleskog and I. Barsoum, "Tension–torsion fracture experiments—Part I: Experiments and a procedure to evaluate the equivalent plastic strain," *International Journal of Solids and Structures*, vol. 50, no. 25-26, pp. 4241-4257, 2013.

[22] Z. Xue, J. Faleskog and J. W. Hutchinson, "Tension–torsion fracture experiments – Part II: Simulations with the extended Gurson model and a ductile fracture criterion based on plastic strain," *International Journal of Solids and Structures,* vol. 50, no. 25-26, pp. 4258-4269, 2013.

[23] M. Scales, N. Tardif and S. Kyriakides, "Ductile failure of aluminum alloy tubes under combined torsion and tension," *International Journal of Solids and Structures,* Vols. 97-98, pp. 116-128, 2016.

[24] K. Nahshon and Z. Xue, "A modified Gurson model and its application to punch-out experiments," *Engineering Fracture Mechanics,* vol. 76, pp. 997-1009, 2009.

[25] U. Prahl, S. Papaefthymiou, V. Uthaisangsuk, W. Bleck, J. Sietsma and S. Van der Zwaag, "Micromechanic-based modelling of properties and failure of multiphase steels," *Computational Materials Science,* vol. 39, no. 1, pp. 17-22, 2007.

[26] Z. Xue, M. G. Pontin, F. Zok and J. W. Hutchinson, "Calibration procedures for a computational model of ductile fracture," *Engineering Fracture Mechanics,* vol. 77, no. 3, pp. 492-509, 2010.

[27] "ASTM A370-17 Standard Test Methods and Definitions for Mechanical Testing of Steel Products," American Society of Testing and Materials, 2017.

[28] Z. L. Zhang and M. Hauge, "On the Gurson Micromechanical Parameters," in *Fatigue and Fracture Mechanics: Twenty-Ninth Volume*, West Conshohocken, PA, American Society for Testing and Materials, 1999.

[29] Hibbitt, Karlsson and Sorensen, ABAQUS/Explicit User's manual, Version 6.2, Pawtuvket, R.I.: Hibbitt, Karlsson and Sorenson Inc., 2001.

[30] M. K. Nielsen, "Predicting ductile tearing of additively manufactured 316L stainless steel," *International Journal of Fracture,* vol. 218, no. 1, pp. 195-207, 2019.

[31] L. Xia, C. F. Shih and J. W. Hutchinson, "A computational approach to ductile crack growth under large scale yielding conditions," *Journal of the Mechanics and Physics of Solids*, vol. 43, no. 3, pp. 389-413, 1995.

[32] A. S. Gullerud, X. Gao, R. H. Dodds Jr and R. Haj-Ali, "Simulation of ductile crack growth using computational cells: numerical aspects," *Engineering Fracture Mechanics,* vol. 66, no. 1, pp. 65-92, 2000.

[33] R. Andersen, J. Londono, P. Woelke and K. Nielsen, "Fundamental differences between plane strain bending and far-field plane strain tension in ductile plate failure," *Journal of the Mechanics and Physics of Solids,* Vols. 141, August 2020,, no. 103960, 2020.

[34] Y. Liu, Z. Lian, T. Shi and P. Sang, "Application of Fracture Mechanics for Evaluation and Improvement of Downhole Perforating Tools," *Engineering Failure Analysis,* vol. 97, pp. 589-604, 2019.

[35] J. Lemaitre, "A continuous damage mechanics model for ductile fracture," *Journal of Engineering Materials and Technology,* vol. 107, no. 1, pp. 83-89, 1985.

[36] J. L. Chaboche, "Continuum damage mechanics: Part I - General concepts," *Journal of Applied Mechanics,* vol. 55, no. 1, pp. 59-64, 1988.

Table 1. Gauge length of virtual extensometer in notch root

Notch size [mm]	Virtual Extensometer gauge length [mm]	Nominal axial strain at notch root [%] (Tension test)	Shear strain at notch root [%] (Torsion test)
1.0	0.5	16.2	100
3.0	1.0	17.9	100
9.0	1.0	18.8	110

Table 2. Calibrated parameter sets

Set ID	HC	f_0	f_c	f_f	k_ω
Set 1	High	0.009	0.075	0.075	2.5
Set 2	Low	0.009	0.065	0.065	1.75
Set 3	High	0.009	0.065	0.065	1.8
Set 4	Low	0.009	0.065	0.065	1.4

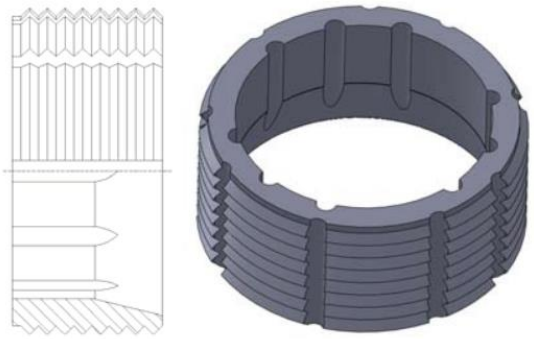

a) Schematic of downhole tool with protruding teeth [2]

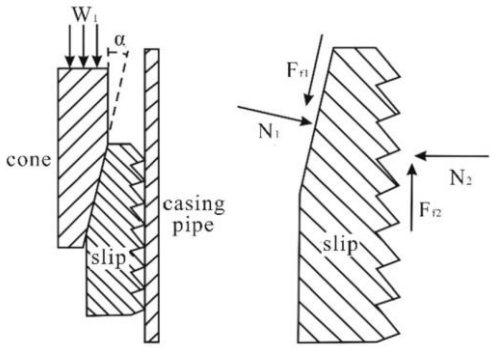

b) Schematic of the setting process [3]

Fig. 1. Setting process schematic from [2] & [3]. The schematic shows the tool setting on casing pipe, which is achieved by indentation of slips into the casing wall.

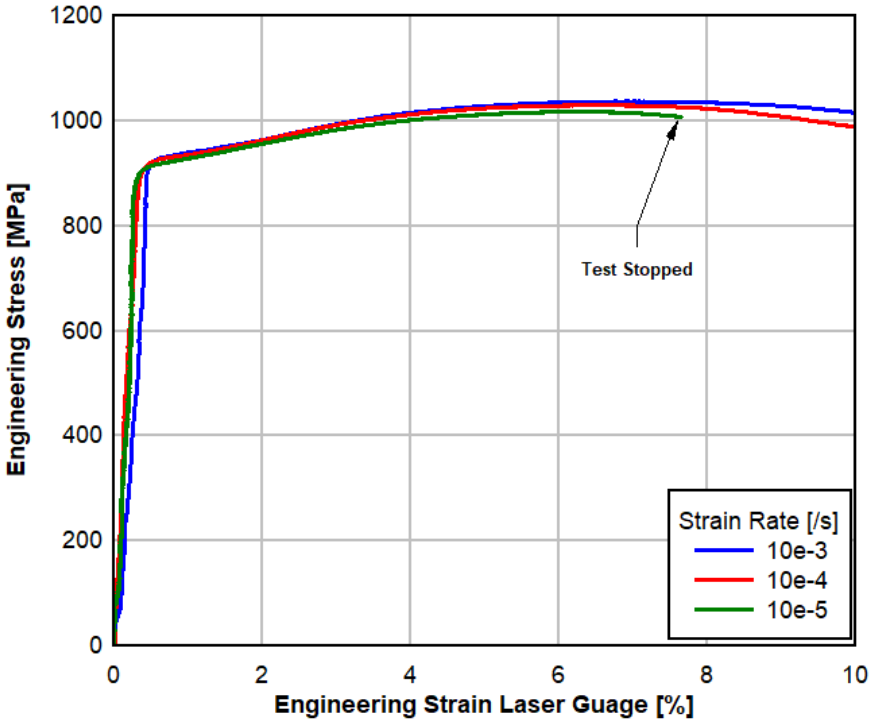

Fig. 2. Uniaxial tensile response from 3 round dogbone (RDB) specimens

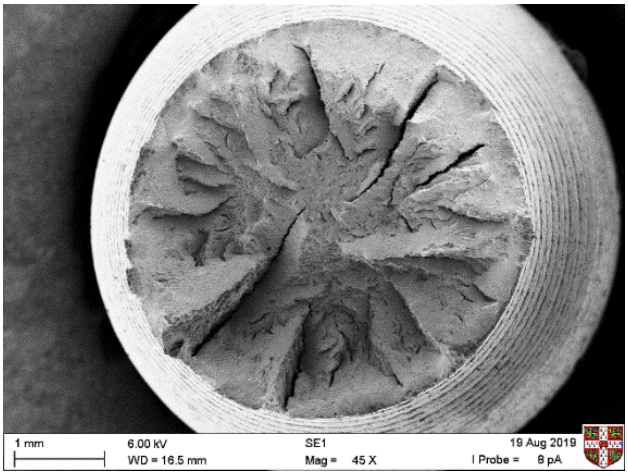

Fig. 3. Plan view of fracture surface, for test of strain rate 10^{-4} s^{-1}.

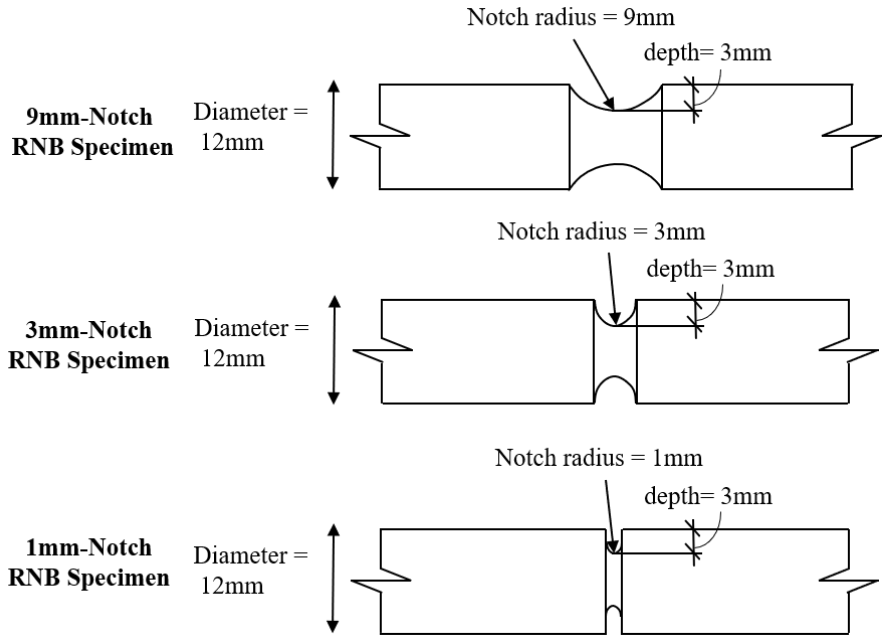

Fig. 4. Round notched bar (RNB) specimen geometries

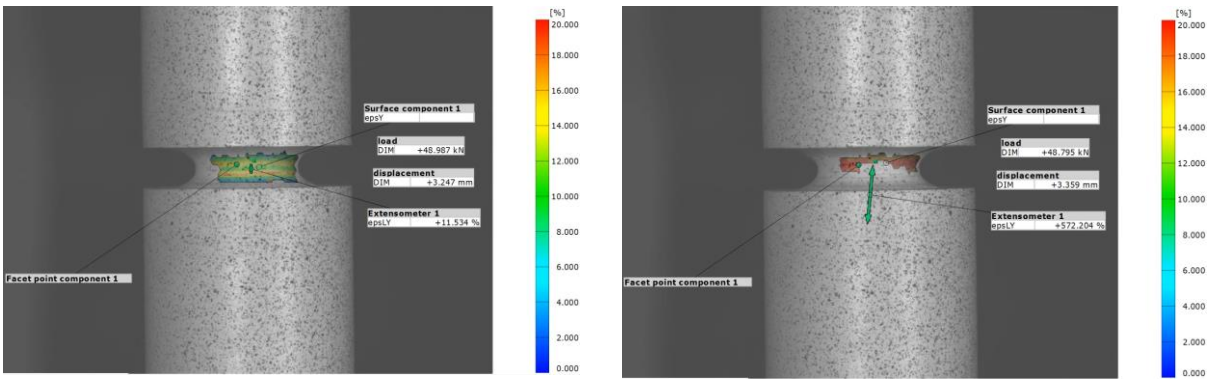

(a) R=1mm notch test DIC image at localization

(b) R=1mm notch test DIC image at failure

Fig. 5. RNB R=1mm notch test DIC images at (a) localization and (b) failure

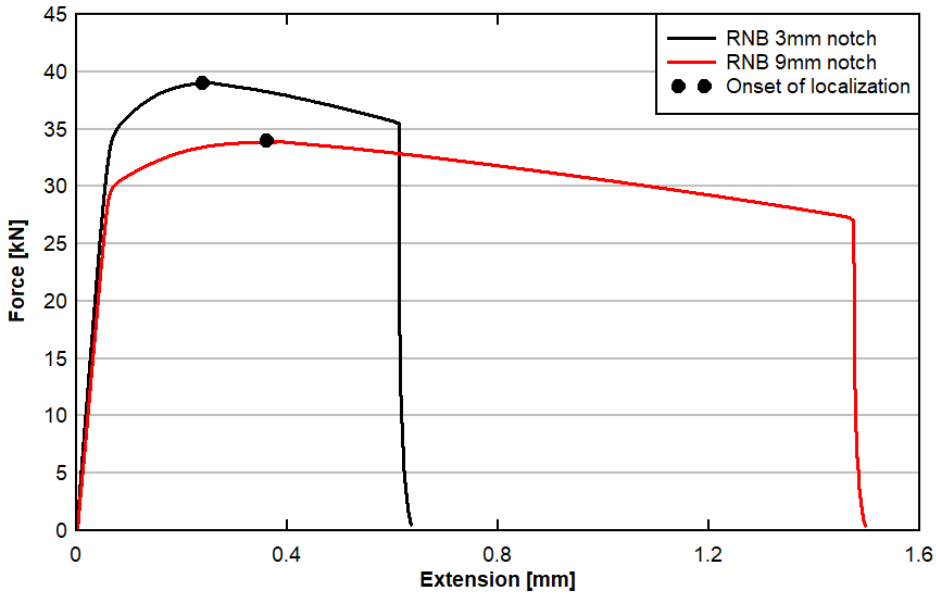

Fig. 6. Load versus extension for R=3mm and R=9mm round notched bars (RNBs) in tension

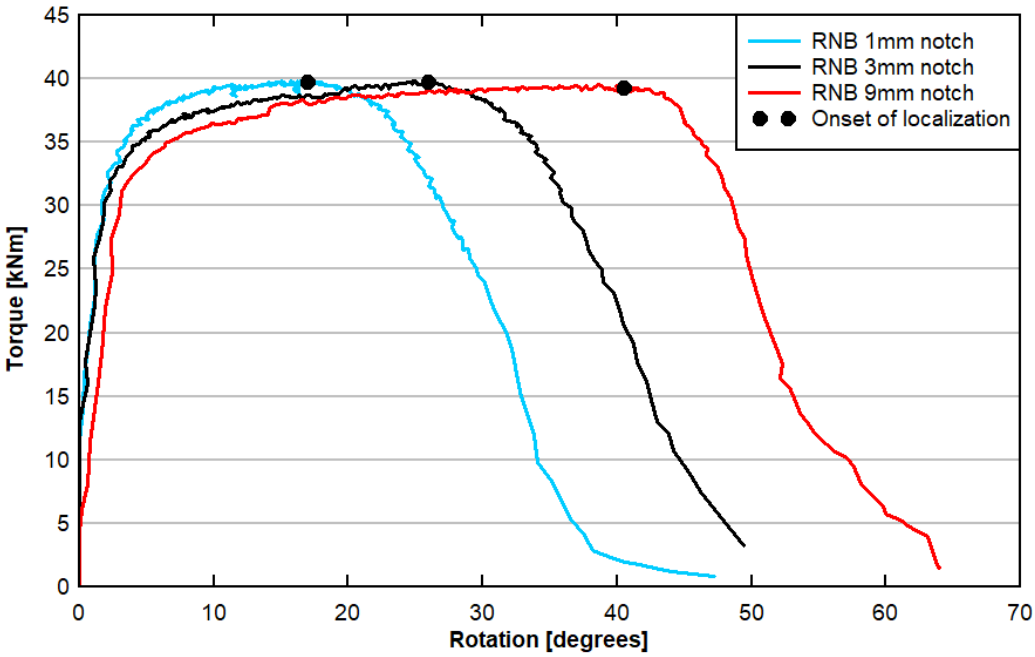

Fig. 7. Torsion test results, torque versus end rotation of specimen

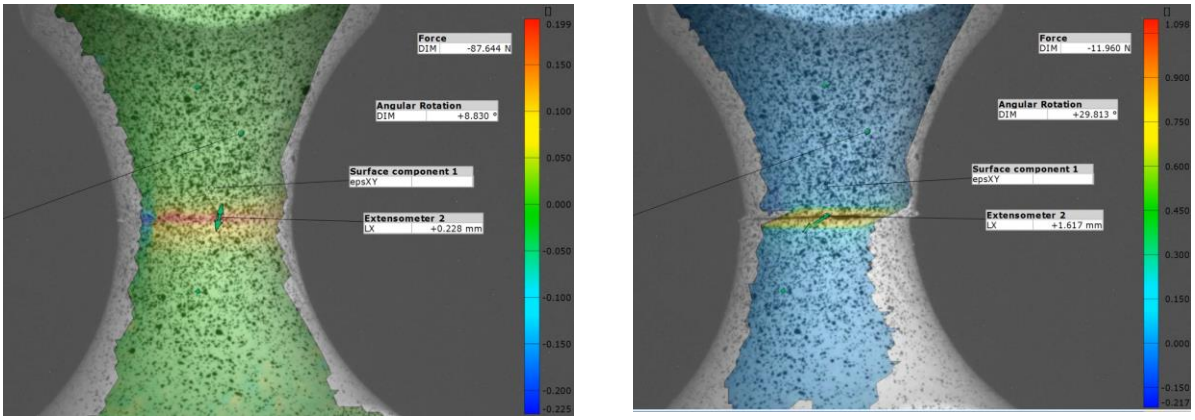

(a) R=9mm notch test DIC image at localization (b) R=9mm notch test DIC image at failure

Fig. 8. RNB R=9mm notch test DIC images at (a) localization and (b) failure

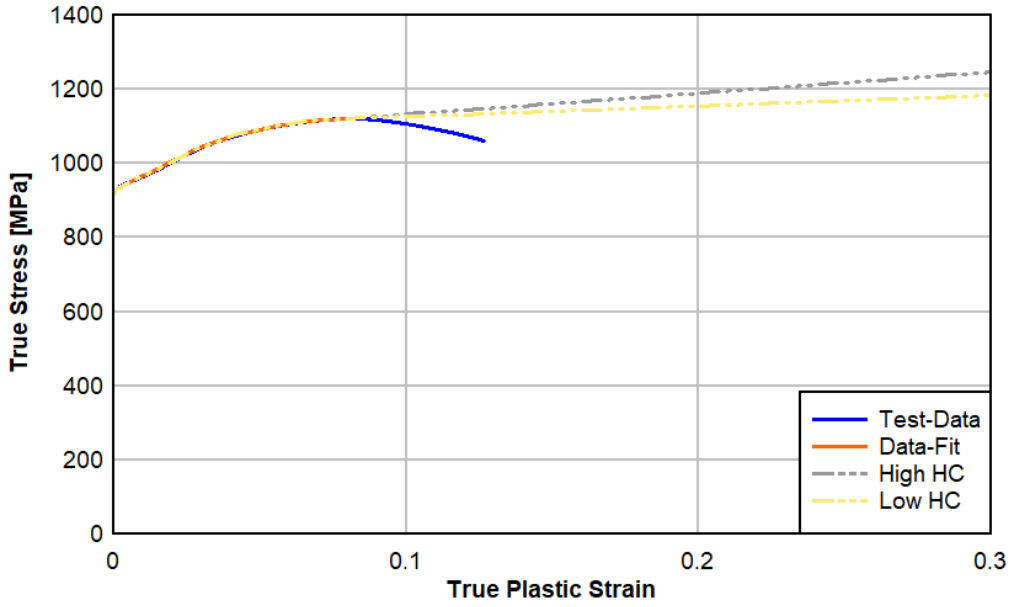

Fig. 9. Extrapolated Hardening Curves

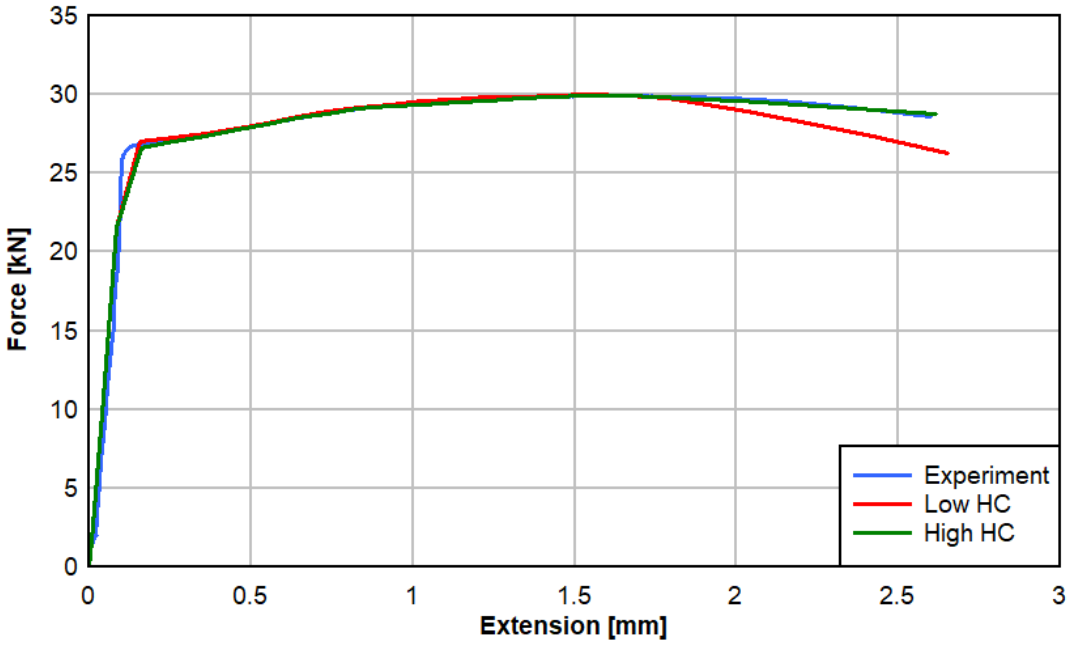

Fig. 10. RDB comparison of hardening curves

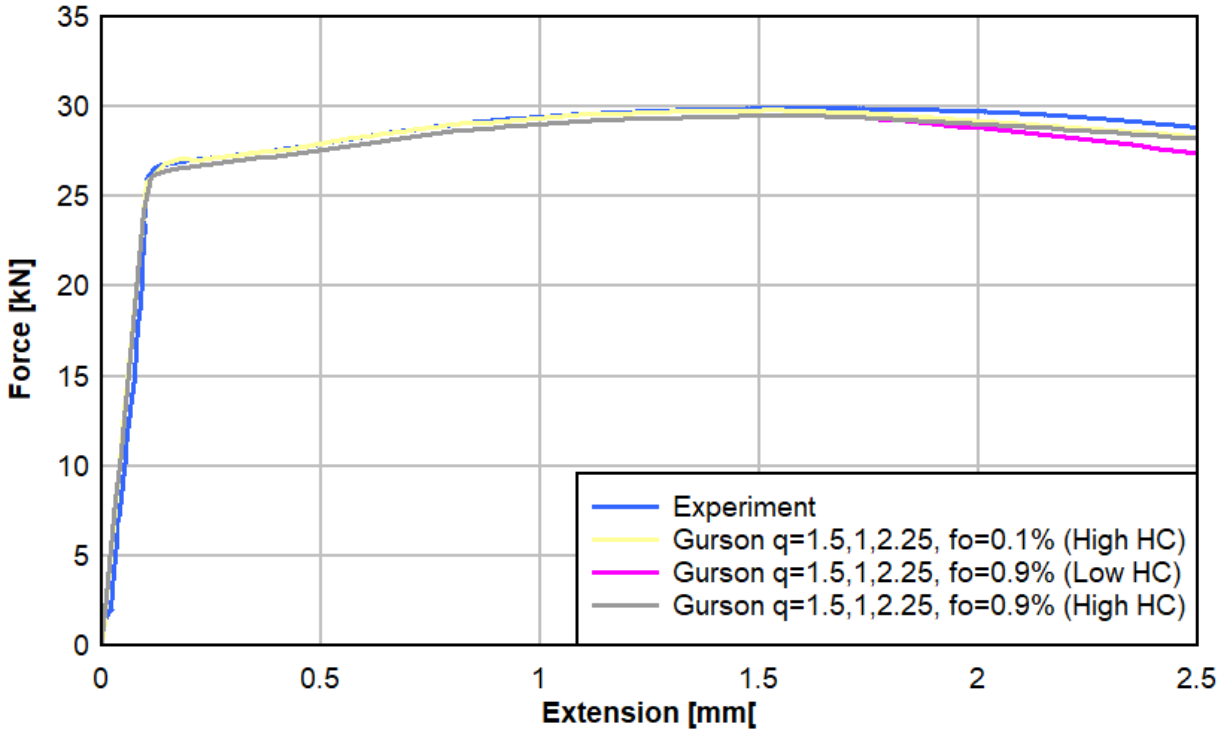

Fig. 11. Force displacement response of RDB simulations

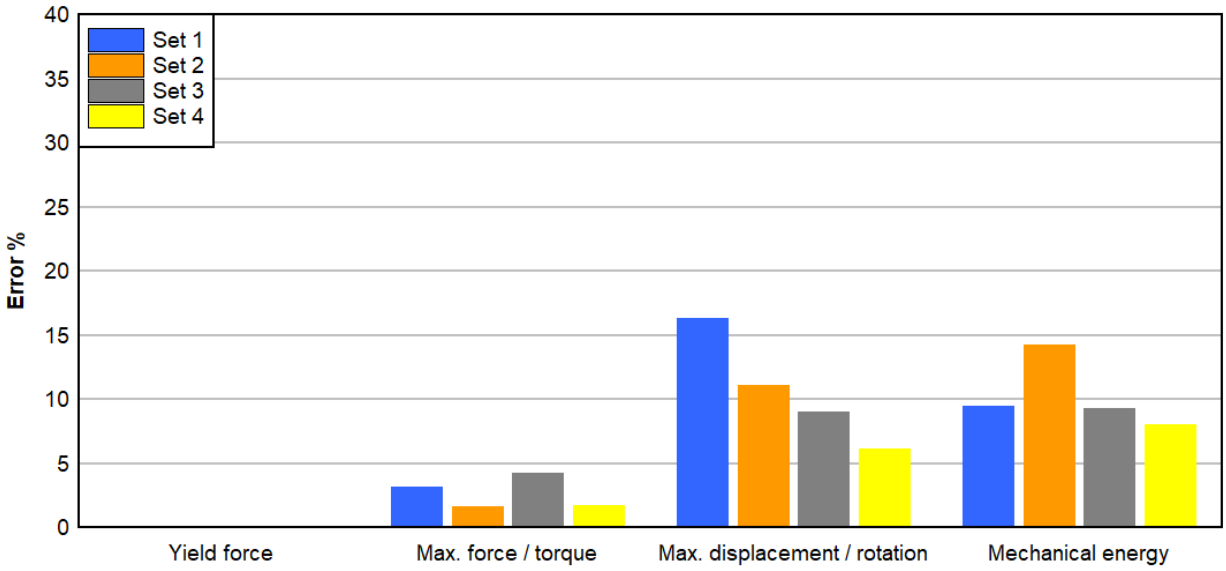

Fig. 12. Performance evaluation of calibrated parameter sets

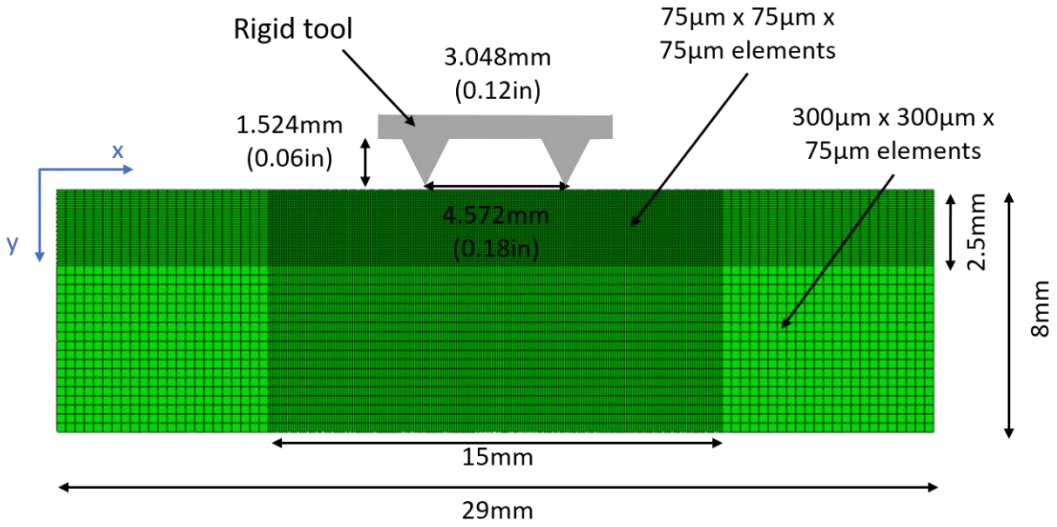

Fig. 13. FEA model of setting representation – mesh and dimensions. The rigid tool indents through casing (motion in y-direction), then shears through (motion in x-direction). The model has roller supports on the edges in x- and y-directions, and out of plane symmetry boundary conditions.

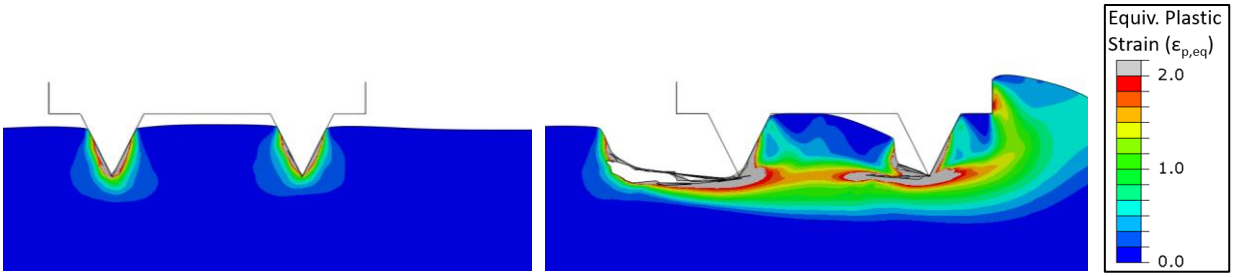

(a) Extended GTN – Indentation – Equiv. plastic strain

(b) Extended GTN – Shear – Equiv. plastic strain

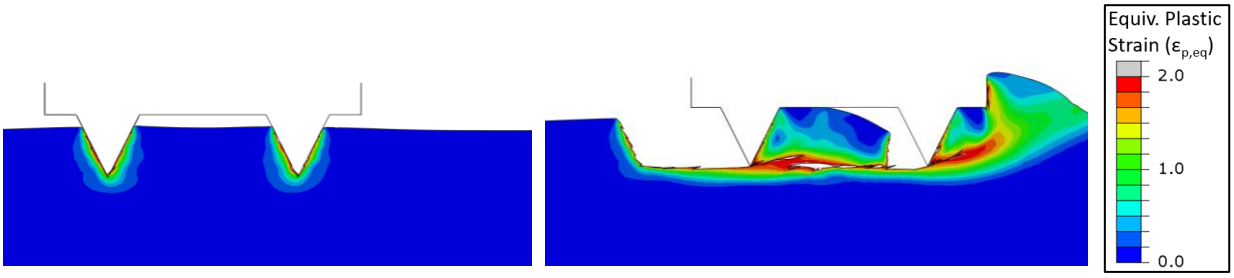

(c) von Mises – Indentation – Equiv. plastic strain

(d) von Mises – Shear – Equiv. plastic strain

Fig. 14. Equivalent Plastic Strains with: (a) extended GTN model after 80% indentation, (b) extended GTN model after shear, (c) von Mises model after 80% indentation and (d) von Mises model after shear. The extended GTN model uses the Set 4 calibrated parameters and the von Mises model uses the Low HC curve.

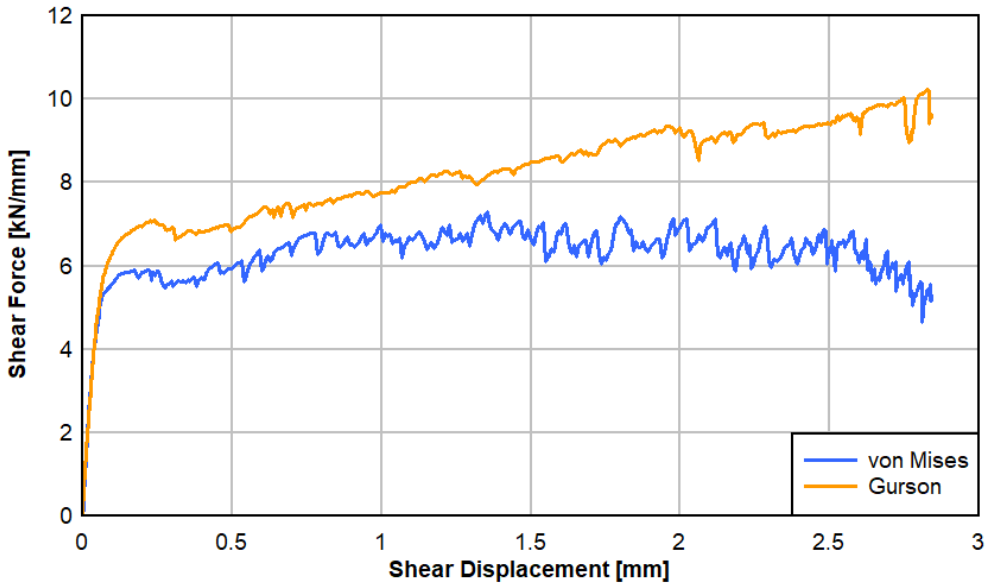

Fig. 15. Shear force vs shear displacement response of setting simulation with extended Gurson and von Mises models. The extended GTN model uses the Set 4 calibrated parameters and the von Mises model uses the Low HC curve.

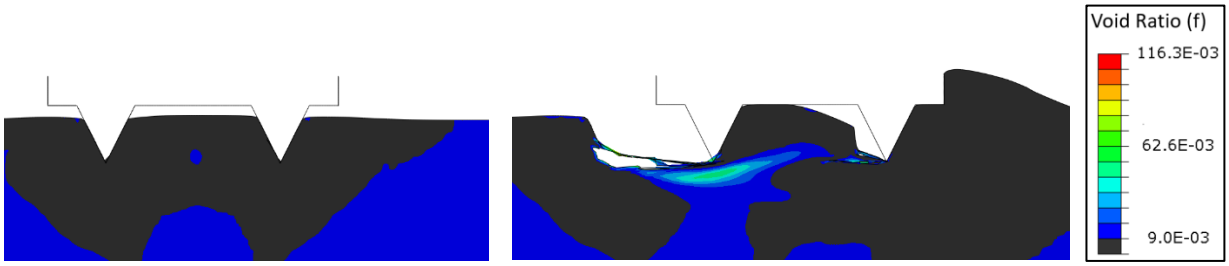

(a) With void closure – Indentation – Void ratio

(b) With void closure – Shear – Void ratio

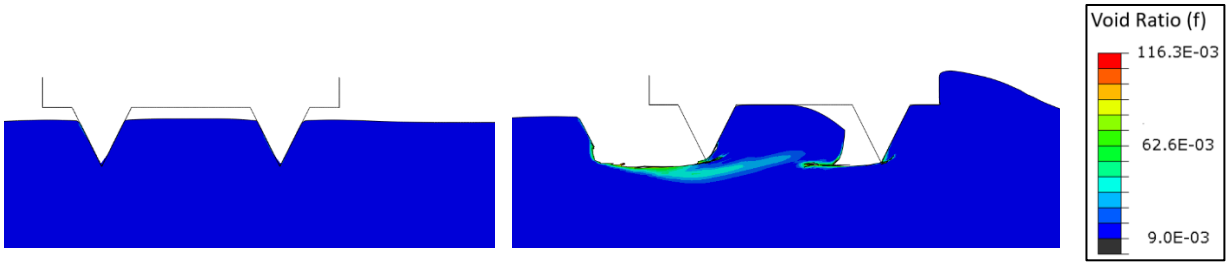

(c) No void closure – Indentation – Void ratio

(d) No void closure – Shear – Void ratio

Fig. 16. Void ratio with: (a) extended GTN model after 80% indentation with possibility of void closure, (b) extended GTN model after shear with possibility of void closure, (c) extended GTN model after 80% indentation with no void closure allowed, (d) extended GTN model after shear with no void closure allowed. The extended GTN model uses the Set 4 calibrated parameters and the von Mises model uses the Low HC curve.

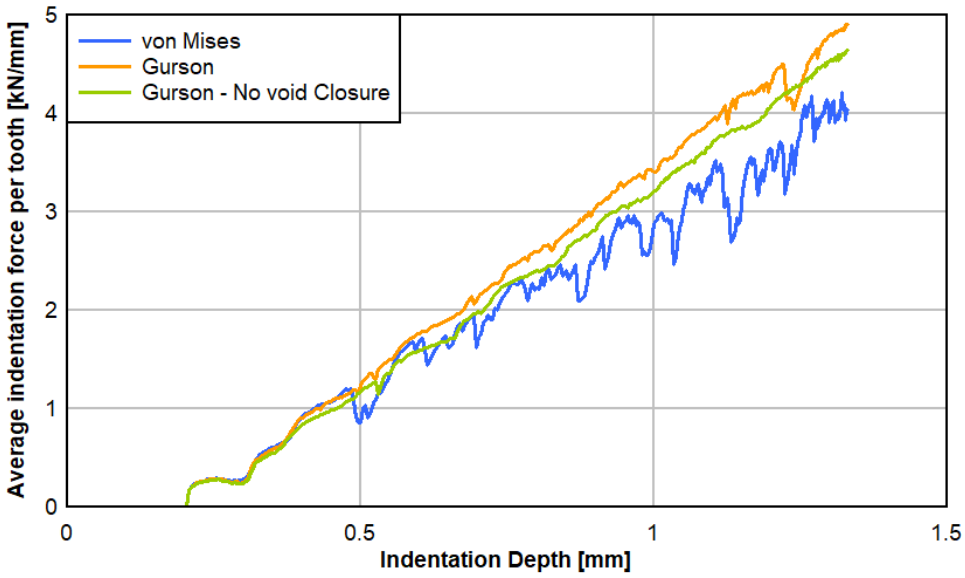

Fig. 17. Indentation force vs indentation depth calculated from three models: von Mises model, extended GTN model with void closure, and extended GTN model without void closure. Results presented are from two-tooth simulation. The extended GTN model uses the Set 4 calibrated parameters and the von Mises model uses the Low HC curve.

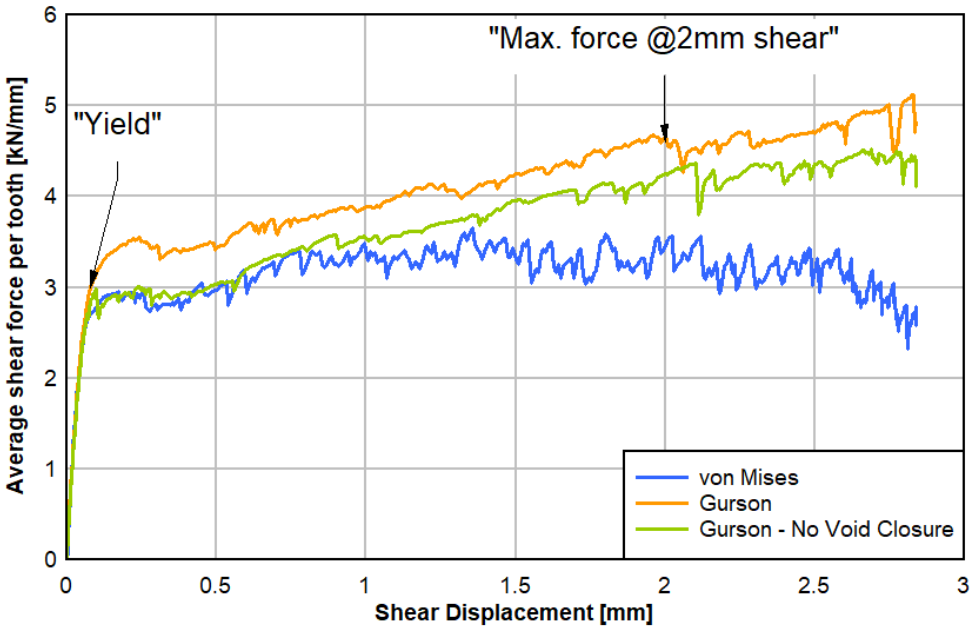

Fig. 18. Shear force vs shear displacement calculated from three models: von Mises model, extended GTN model with void closure, and extended GTN model without void closure . Results presented are from two-tooth simulation. The extended GTN model uses the Set 4 calibrated parameters and the von Mises model uses the Low HC curve.

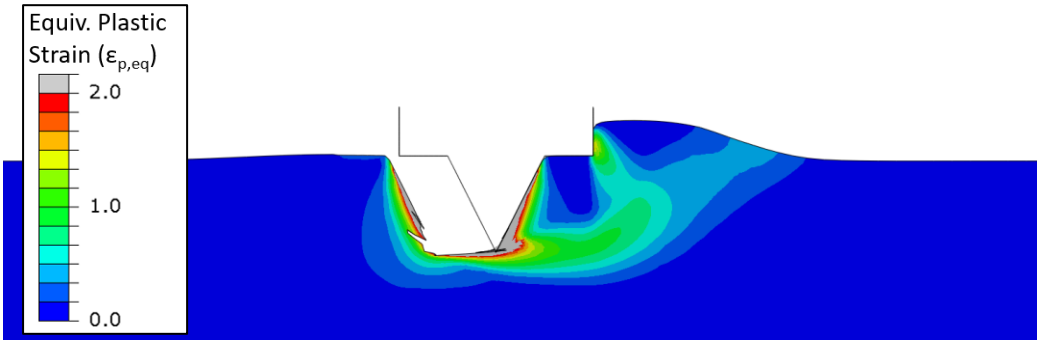

(a) 1 Tooth

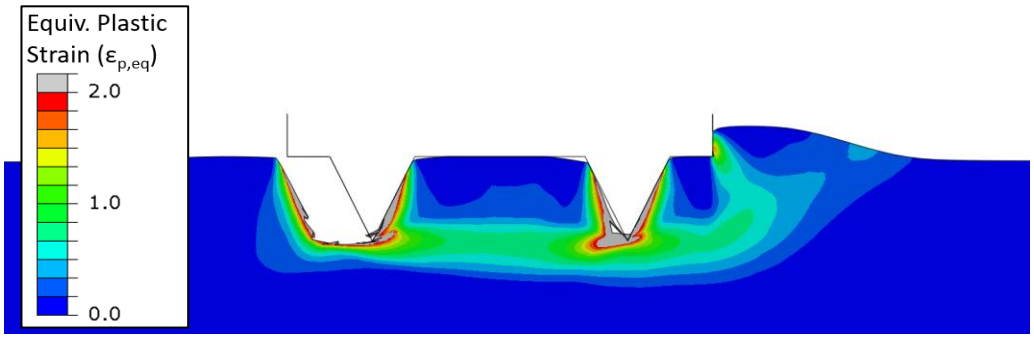

(b) 2 Teeth

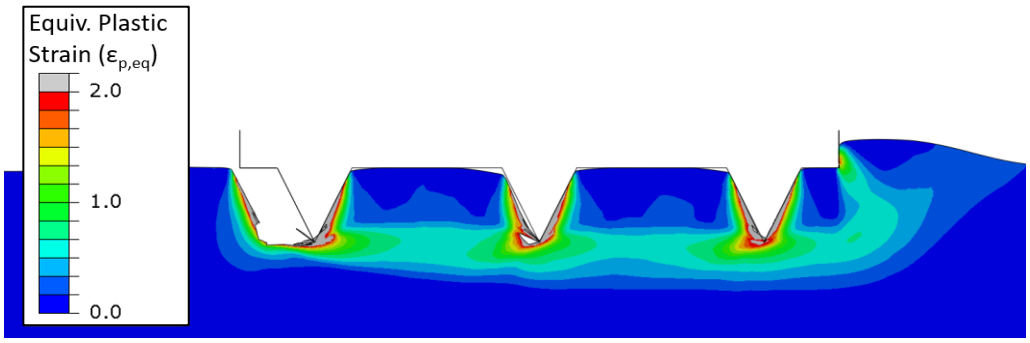

(c) 3 Teeth

Fig. 19. Equivalent plastic strain in (a) 1, (b) 2 and (b) 3 tooth models. All models feature 100% indentation. The simulations use the extended GTN model with Set 4 calibrated parameters.

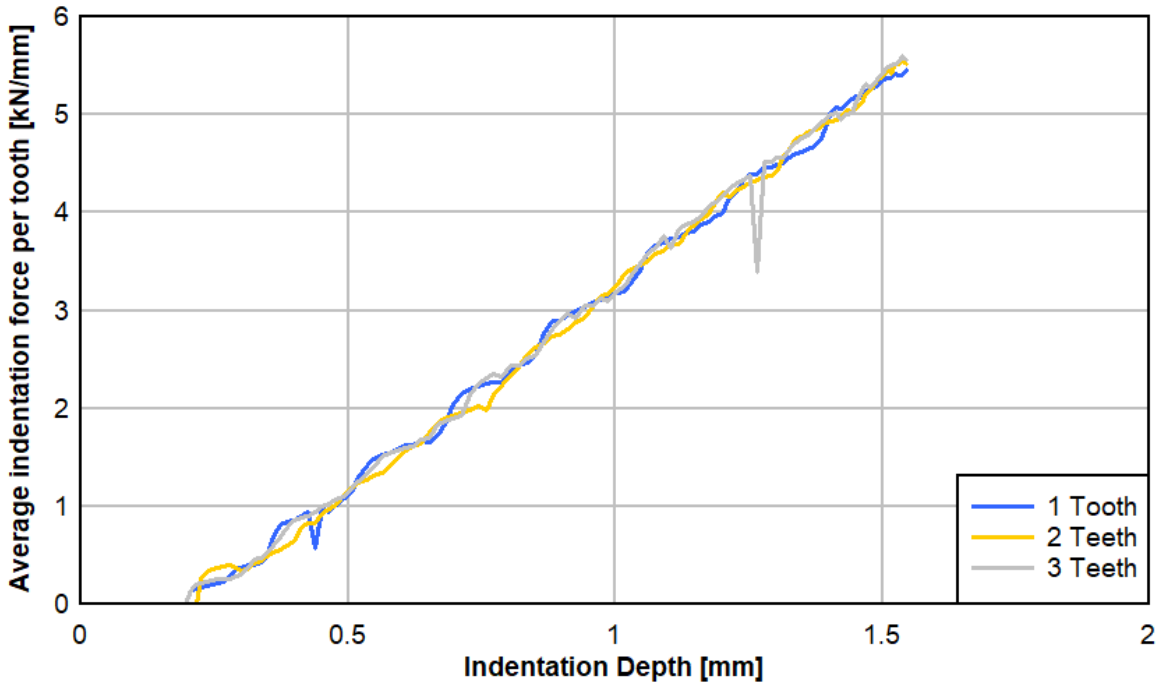

(a) Normalized indentation force per tooth vs indentation depth

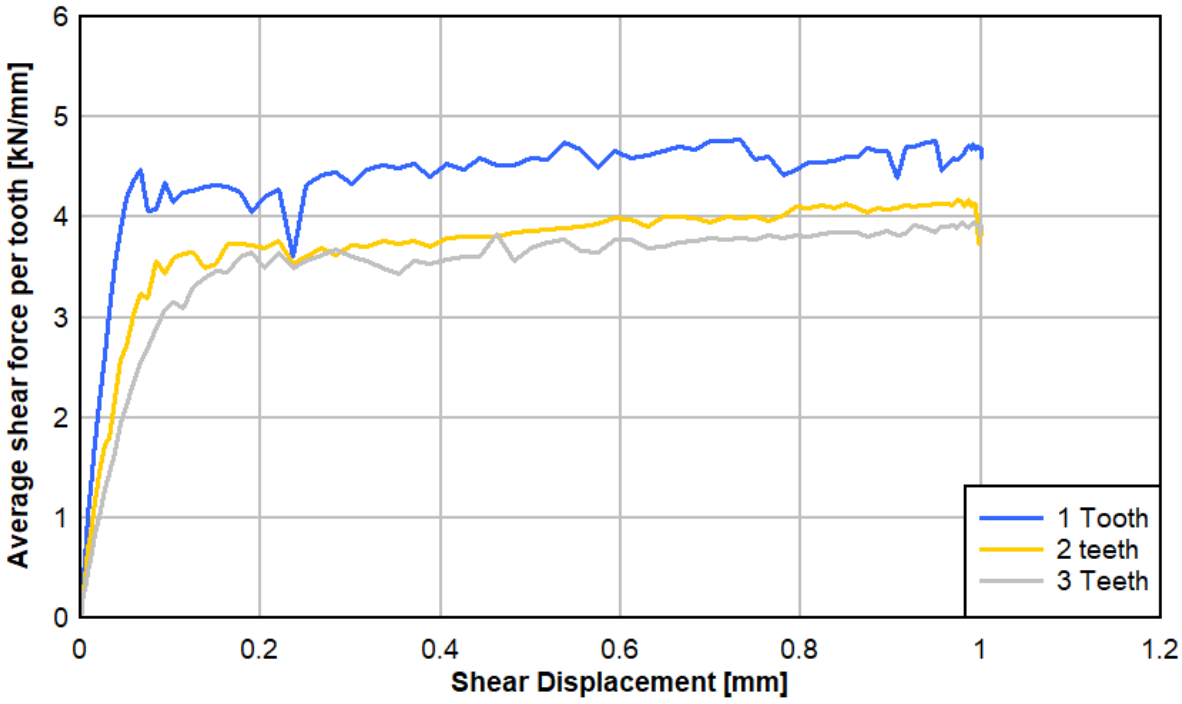

(b) Normalized shear force per unit width per tooth vs shear depth

Fig. 20. Force displacement response per tooth in (a) indentation and (b) shear. The simulations use extended GTN model with the Set 4 calibrated parameters.

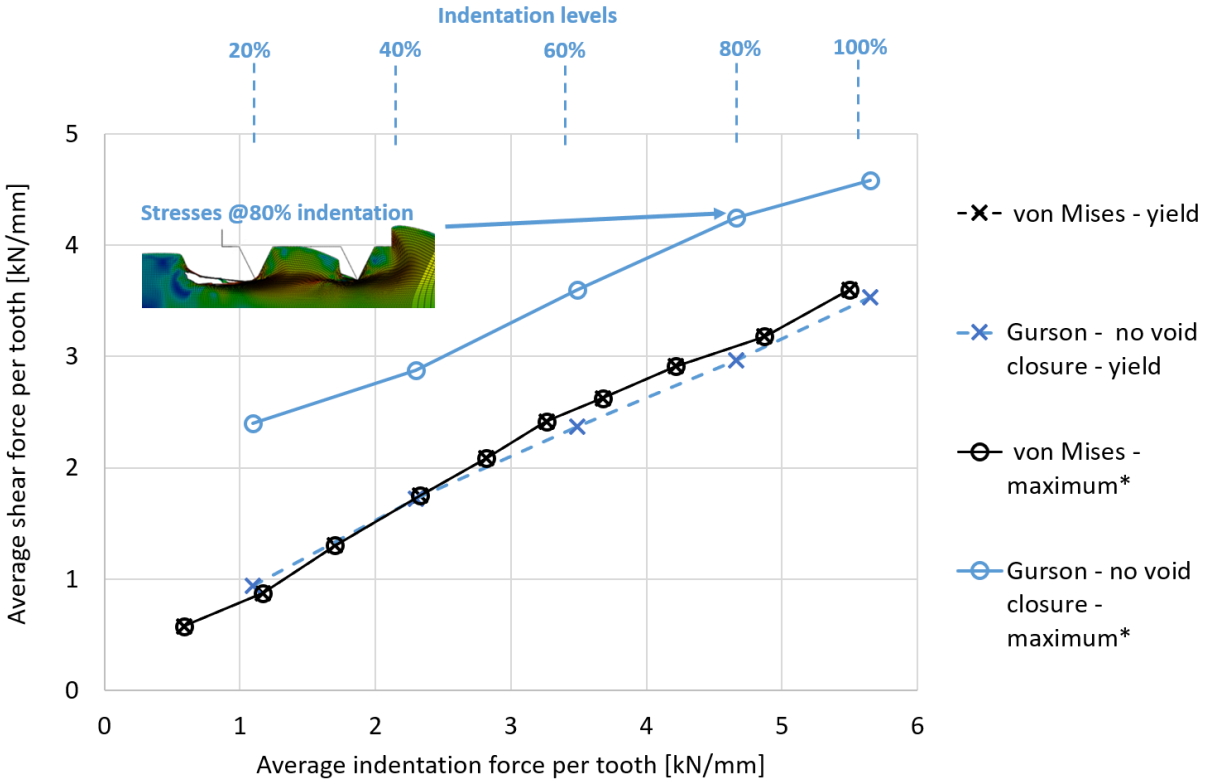

Fig. 21. Connection strength vs indentation force for the two-teeth model

Supplemental Material

A – Experimental Setup

Specimens were machined from a 0.5m length of AISI 4140 casing (outer diameter =6.85in., wall thickness = 0.625in.). Specimens were aligned with the axis of the casing in the longitudinal direction. Tension tests were performed using a screw-driven test machine, with serrated wedge grips of 100kN load capacity. The tensile axial load was measured using the load cell of the test machine. The relative displacement of the ends of the specimen were measured by the displacement transducer of the test machine. In addition, a laser gauge, clip gauge and a 3D Digital Image Correlation (DIC) system were employed to measure the axial strain.

Torsion tests were performed using a suitable instrumented torsion machine: a torque was applied to the ends of each specimen by a geared system. The specimens had ends of square cross-section 12mm x 12mm in order for the torsional load to be transmitted from the test machine. The torsional load was measured via a lever arm of length 0.45m, with the end of the lever arm bearing on a 2kN compression load cell. This compressive load was recoded along with images of the notch root. The relative rotation of the 2 ends of the specimen were measured by a potentiometer and the rotation was recorded. The 3D DIC system was employed to measure the shear strain at the notch root during each test under increasing relative rotation of the 2 ends of the specimen.

B – Finite Element Modeling and Calibration Results

The RDB specimen was modeled using an axisymmetric model as shown in Fig. B1. The element size in the gauge section was 50 μm x 50 μm. The loading was applied through incremental displacement of the boundary at a constant velocity.

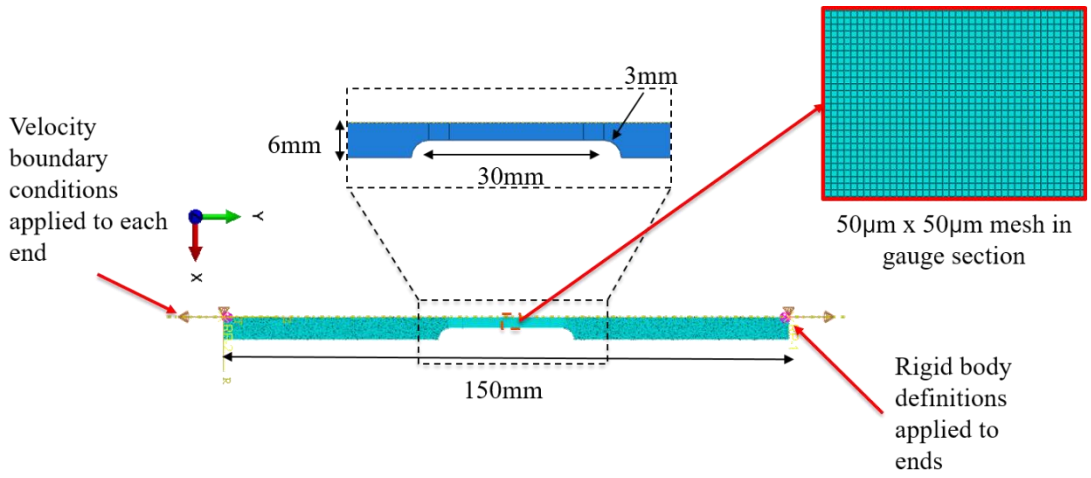

Fig. B1. RDB finite element model and mesh

The abbreviations RNB1, RNB3 and RNB9 are used to denote the 1mm notch, 3mm notch and 9mm notch specimens, respectively. As shown in Fig. B2, the RNB-tension specimens were modeled using axisymmetric models. The loading is applied as incremental boundary displacement (constant velocity) and the mesh size in the notch section is 40µm x 6µm.

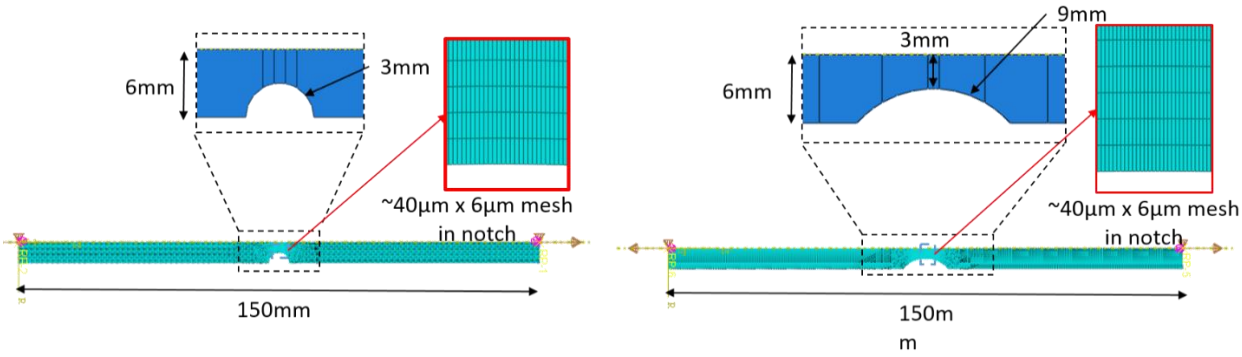

(a) RNB3 tension model (b) RNB9 tension model

Fig. B2. Tension finite element models and mesh for (a) RNB3 and (b) RNB9

The nature of the torsion loading and the stress state developing inside the specimen lead to the need to model the specimen in full three-dimensional detail as shown in Fig. B3. Relatively larger element sizes are used in the notch zone to improve the computational cost, the element size in the circumferential direction is kept at 150-170 µm.

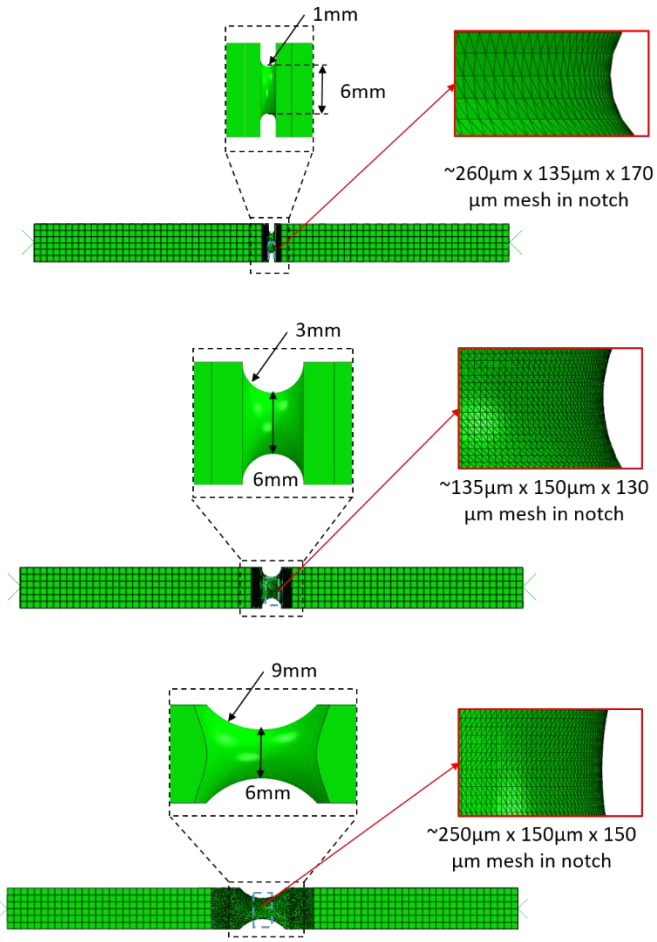

Fig. B3. RNB Torsion finite element models and meshes for (a) RNB1, (b) RNB3 and (c) RNB9

B.1. RNB Tension: RNB3 & RNB9

The force-displacement resulting from the calibrated shear-extended GTN model with parameters defined from the four sets in Table 4 are compared against the experimental data in Figs. B4 and B5 for RNB3 and RNB9 respectively. Several key observations can be drawn from these plots:

- The four sets provide a reasonable match to the experimental response except the results from Set 3 which tends to overestimate the maximum displacement
- The variation of kw (comparing Set 2 to Set 4) has an insignificant effect on the model response
- Both of the High HC and Low HC sets fall on the top of each other for RNB9, but there is a more significant difference between High HC and Low HC in RNB3 results. This

indicates that the choice of the hardening curve has a larger influence on more localized stress states in smaller notch sizes.

The pre-fracture stress localization observed in the model is compared to DIC images in Fig. B6 for the R=3mm notch size.

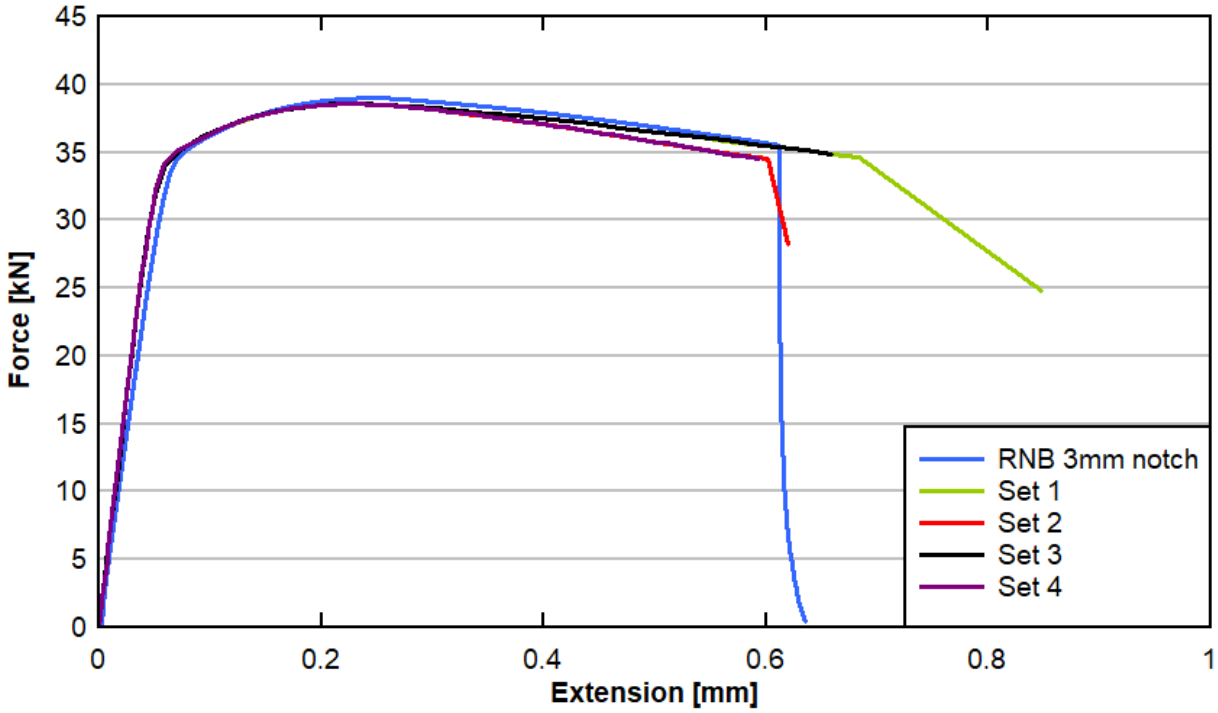

Fig. B4. RNB3 tension simulation force-displacement response

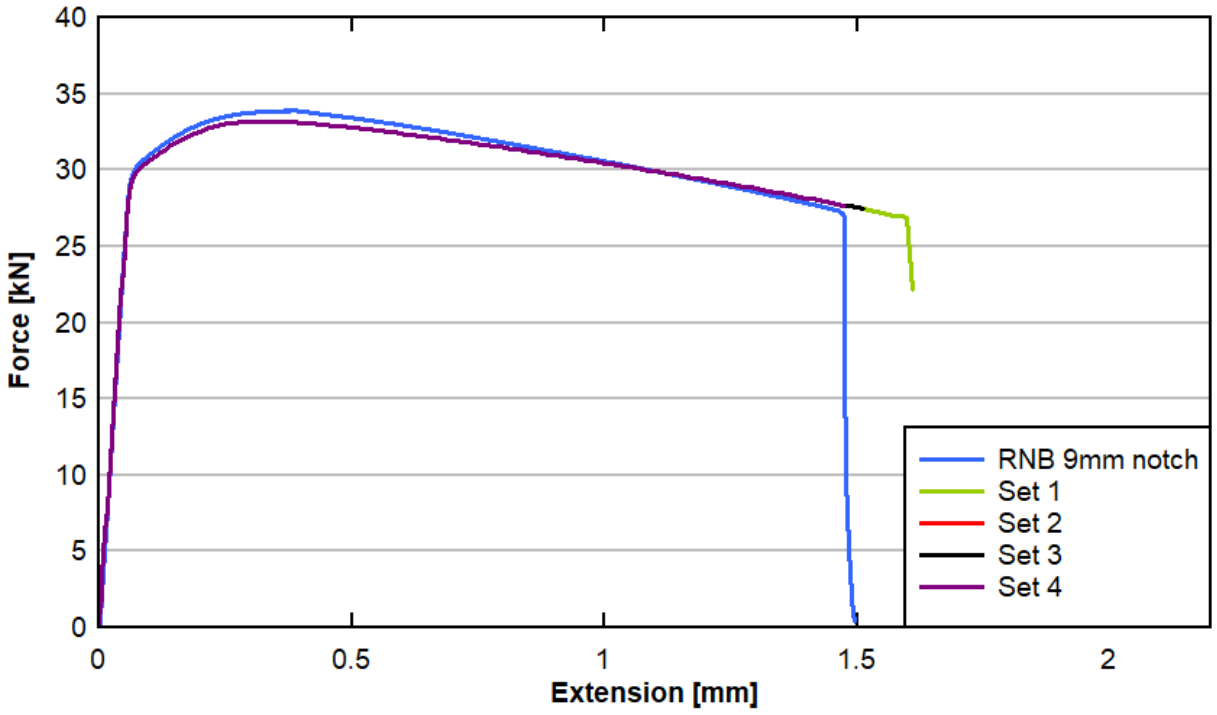

Fig. B5. RNB9 tension simulation force-displacement response

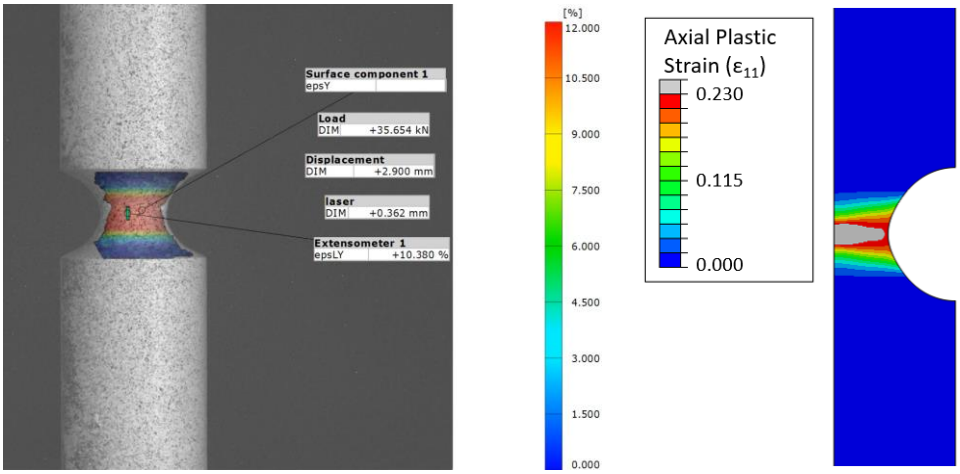

(a) RNB3 Experiment (b) RNB3 Simulation

Fig. B6. Comparison of (a) experiment and (b) simulation at localization (RNB3)

B.2. RNB Torsion: results from RNB9, RNB3 and RNB1

Torque-rotation response of the 1mm, 3mm and 9mm models is compared to experimental data in Figs. B7, B8 and B9 respectively.

Several key observations can be made from the torque-rotation plots:

- increasing k_{ω} has a direct and significant effect on defining the final portion of the curve, more specifically, the rotation at which abrupt damage kicks in and torque capacity drops
- unlike all tension results, both High HC and Low HC sets tend to overshoot the torque response, the Low HC sets provide a better match
- the response from all four sets tends to show earlier failure that experimental response as the notch size decreases

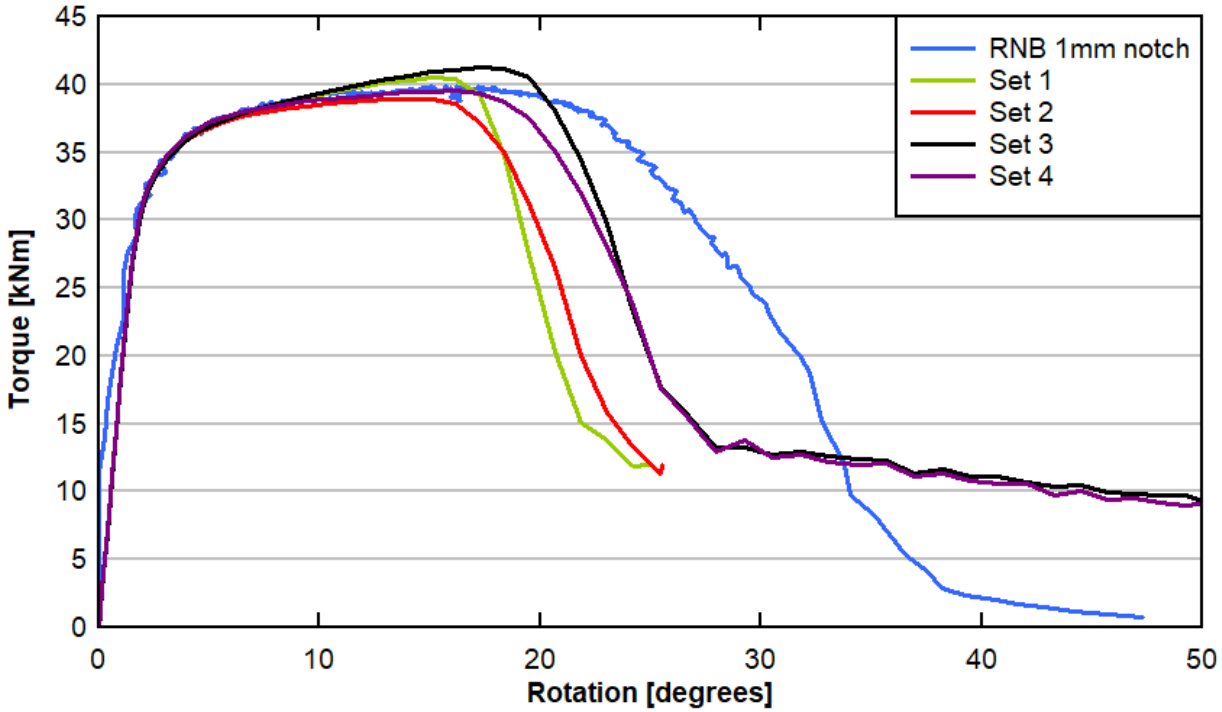

Fig. B7. RNB1 torsion simulation response

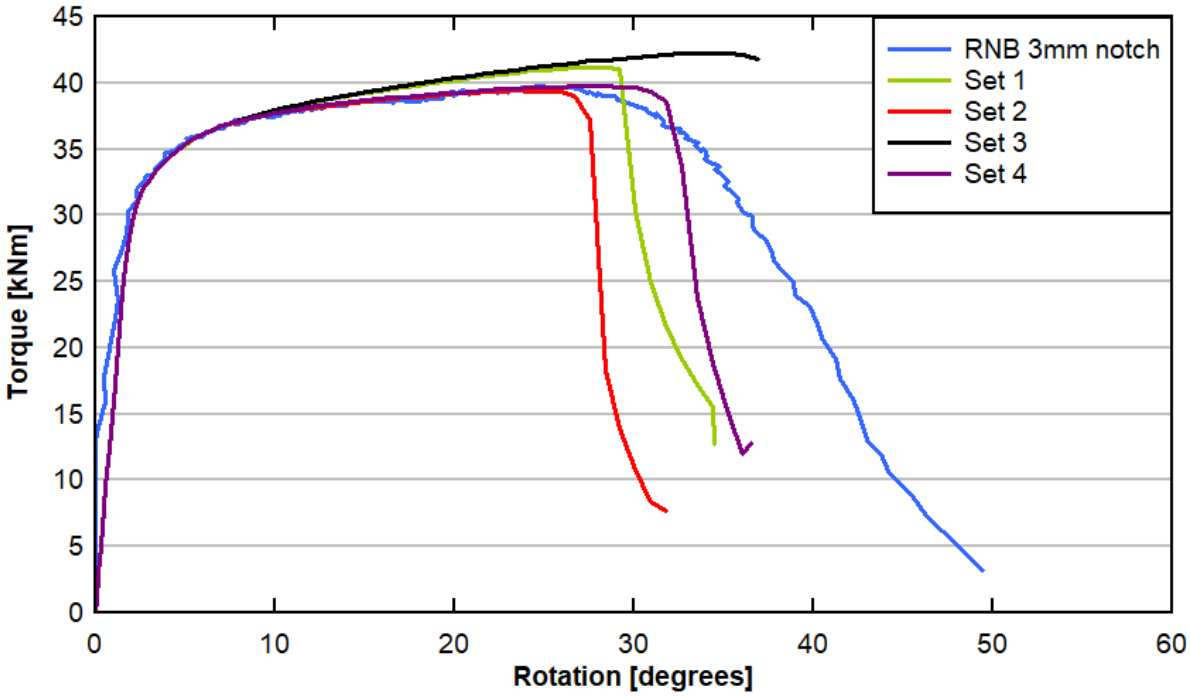

Fig. B8. RNB3 torsion simulation response

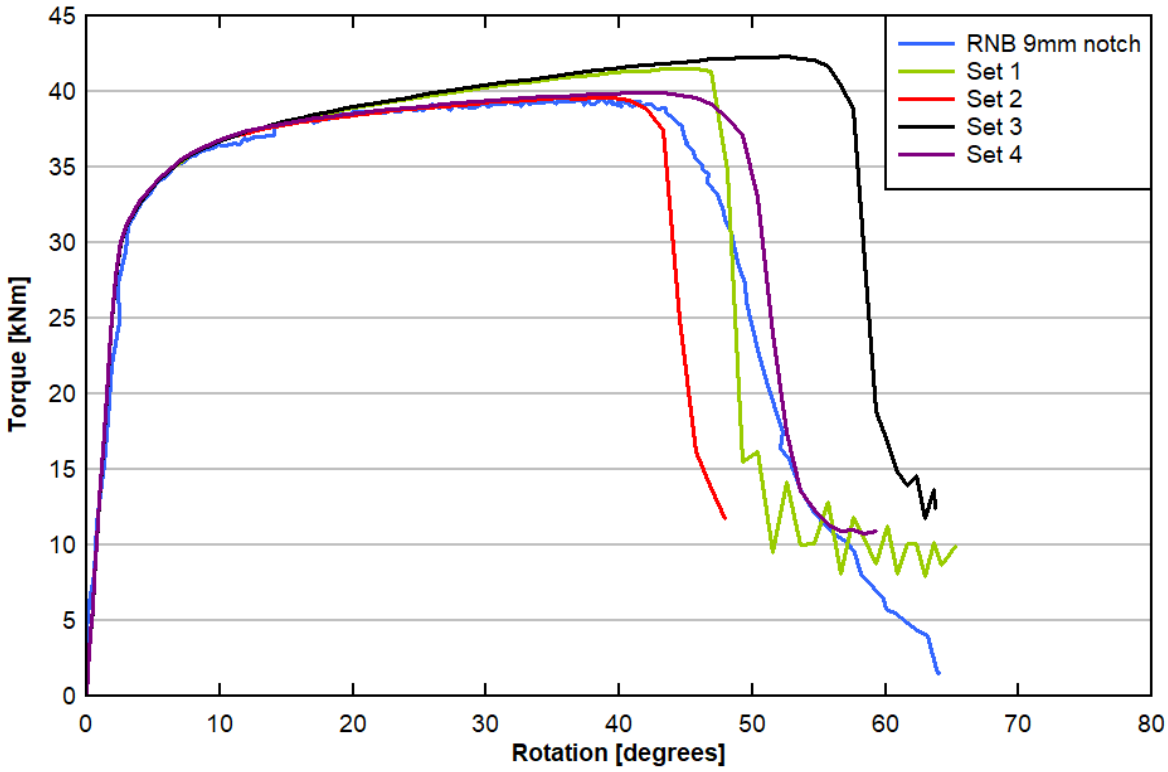

Fig. B9. RNB9 torsion simulation response